Aalto University
School of Science
Master's Programme in Life Science Technologies

Pauliina Hirvi

Generating head models for diffuse optical tomography of the child brain

Master's Thesis
Espoo, January 7, 2019

Supervisor: Prof. Risto J. Ilmoniemi
Advisors: Dr. Ilkka Nissilä, Department of Neuroscience and Biomedical Engineering
Prof. Nuutti Hyvönen, Department of Mathematics and Systems Analysis

Aalto University
School of Science

Aalto University
School of Science
Master's Programme in Life Science Technologies

ABSTRACT OF
MASTER'S THESIS

Author:	Pauliina Hirvi		
Title:	Generating head models for diffuse optical tomography of the child brain		
Date:	January 7, 2019	**Pages:**	viii + 59
Major:	Biomedical Engineering	**Code:**	SCI3059
Supervisor:	Prof. Risto J. Ilmoniemi		
Advisors:	Dr. Ilkka Nissilä Prof. Nuutti Hyvönen		

Diffuse optical tomography (DOT) provides a practical method for studying cortical brain activity in toddlers. In DOT, tissue is illuminated with near-infrared light to estimate the three-dimensional distribution of optical parameter changes that result from the hemodynamic response to neuronal activity. This is an inverse problem where the correctness of the result is very sensitive to the accuracy of the forward solution.

The forward solution requires an optical model of the head, including a segmented anatomical model, locations of the optodes (sources and detectors) and the baseline optical parameters of the tissue types. This thesis presents improved child-friendly methods for generating the optical model.

The first part of the methods is for registering an age-appropriate atlas template to points measured with photogrammetry from the subject's head. The second part enables interpolating the locations of the optodes on the deformed template using the known layout of the measurement probe. The final algorithm performs a Gaussian random search in the parameter space to find the optical parameters.

In this thesis, the first two methods were applied for 17 two-year-olds participating in an affective touch study. The average accuracy of the surface registration was 1.7 mm, and the interpolation reconstructed the optode layout with an average error of 0.6 mm. The probe positions also corresponded to the placements according to the photographs. Further study will combine these models with measurements to estimate the optical parameters of two-year-olds, which current literature does not provide.

Keywords:	affine transformation, anatomical model, brain, diffuse optical tomography, functional imaging, grid search, image registration, near-infrared light, optical parameters, parallel computing, photogrammetry, random search
Language:	English

Aalto-yliopisto
Perustieteiden korkeakoulu
Master's Programme in Life Science Technologies

DIPLOMITYÖN
TIIVISTELMÄ

Tekijä: Pauliina Hirvi

Työn nimi:
Päämallien tuottaminen lasten aivojen diffuusiin optiseen tomografiaan

Päiväys:	7. tammikuuta 2019	**Sivumäärä:**	viii + 59
Pääaine:	Biomedical Engineering	**Koodi:**	SCI3059
Valvoja:	Professori Risto J. Ilmoniemi		
Ohjaajat:	TkT Ilkka Nissilä Professori Nuutti Hyvönen		

Diffuusi optinen tomografia (DOT) on käytännöllinen menetelmä lasten aivokuoren aktivaatioiden tutkimiseen. Aivohermosolujen sähköinen aktivaatio muuttaa paikallista verenkiertoa ja sitä kautta kudoksen optisia ominaisuuksia. DOT-menetelmässä kudosta läpivalaistaan lähi-infrapunavalolla, jotta saadaan kuvattua optisten parametrien muutosten kolmiulotteinen jakauma. Kyseessä olevan käänteisongelman ratkaisu on erittäin herkkä vastaavan suoran ongelman ratkaisun tarkkuudelle.

Suoran ongelman ratkaisemiseksi tarvitaan optinen päämalli, johon kuuluu segmentoitu anatominen malli, optisten kuitujen (valon lähteet ja detektorit) paikat ja kudostyyppien optiset taustaparametrit. Tässä työssä esitetään lapsille suotuisa menetelmäkokonaisuus optisen päämallin tuottamiseksi.

Ensiksi kohdehenkilön ikäluokkaa vastaava atlas-malli rekisteröidään henkilön päänpinnan muotoa vastaavaksi. Pään muoto on esitetty fotogrammetrialla mitattujen pisteiden avulla. Tämän jälkeen kuitujen paikat interpoloidaan mallin pinnalla hyödyntämällä niiden tunnettua sijoittelua mittauspäätteessä. Lopuksi valitaan satunnaisesti joukko optisia parametreja kullekin kudostyypille, ja etsitään simuloitua mittausdataa vastaavia suoran ongelman ratkaisuja tuottavat vaihtoehdot.

Tässä työssä tuotettiin kuitujen paikoilla varustetut anatomiset mallit seitsemälletoista kaksivuotiaalle, jotka osallistuivat hellää kosketusta käsittelevään tutkimukseen. Rekisteröinnin keskimääräinen tarkkuus oli 1.7 mm, ja kuitujen sijoittelu vastasi tunnettua rakennetta keskimäärin 0.6 millimetrin tarkkuudella. Lisäksi mittauspäätteen sijainti ja asento näyttivät samoilta kuin valokuvissa. Muodostettuja malleja käytetään jatkossa todellisten optisten parametrien määrittämiseen, koska näitä arvoja ei löydy vielä kirjallisuudesta.

Asiasanat:	affiinimuunnos, anatominen malli, aivot, diffuusi optinen tomografia, fotogrammetria, funktionaalinen kuvantaminen, hilaoptimointi, kuvarekisteröinti, lähi-infrapunavalo, optiset parametrit, rinnakkaislaskenta, satunnaisoptimointi
Kieli:	Englanti

Acknowledgements

First of all, I thank my instructors Dr. Ilkka Nissilä and Prof. Nuutti Hyvönen: Ilkka, you were always ready for discussion, but gave me the freedom to solve problems myself. Nuutti, your support and encouraging words were essential for me during this process. I also wish to express my gratitude to my supervisor Prof. Risto Ilmoniemi, especially for the motivating feedback session on this thesis. It has been an honor to have you three guiding me.

I am grateful to all current and previous members of the NIRS group, especially Mahlet Zewde and Salla Autti, for being great co-workers. Thank you Dr. Kalle Kotilahti for introducing me to the world of photogrammetry, and Dr. Juha Heiskala for comments on the optical parameters. I also appreciate Ambika Maria and the other co-authors for letting me be part of the affective touch study. Finally, the group thanks Dr. Touko Kaasalainen for letting us use the CT imaging modalities at Meilahti Hospital.

NBE has provided a motivating working environment, where I have had the privilege to be treated as a colleague by people whom I look up to. Especial thanks to Matti Mikkola for being a loyal lunch companion. I am also grateful to Assistant Professor Antti Hannukainen from the Department of Mathematics and Systems Analysis for showing interest in my work.

I acknowledge the computational resources and the related courses provided by the Aalto Science-IT project. I also wish to thank all the students I have assisted during various courses—teaching has been the best way to learn! For enriching my student life, I am grateful to Plätty boards 2015–2017 and the Physicist spexes Limbo, Mielenpuhaltajat and Vive!

Finally, for unconditional support, I thank my four most important loved ones: My parents Kirsti and Harri, Tellu-mummi and Petteri. *Äiti ja isi, tämä työ on omistettu teille!*

Espoo, January 7, 2019

Pauliina Hirvi

Acronyms, Symbols and Toolboxes

Acronyms

CPU	Central processing unit
CSF	Cerebrospinal fluid
CT	Computed tomography
DC	Direct current
DOT	Diffuse optical tomography
FD	Frequency domain
(f)MRI	(Functional) Magnetic resonance imaging
GM	Gray matter
GPU	Graphics processing unit
HbT	Total hemoglobin (concentration)
LPA, RPA	Left and right preauricular points
LRE	Landmark registration error
MAAPE	Mean arctangent absolute percentage error
MAD	Mean absolute difference
MC	Monte Carlo methods
MCX	Monte Carlo eXtreme software
MED	Mean Euclidean distance
MSE	Mean squared error
NAS	Nasion
NIR(s)	Near-infrared light (spectroscopy)
NRE	Nasion registration error
pMC	Perturbation Monte Carlo method
RMSE	Root mean square error
RTE	Radiative transfer equation
SDD	Source–detector distance
SRE	Surface registration error
std	Standard deviation
WM	White matter

Symbols

A	(Modulation) Amplitude
d	Step length in parameter grid
g	Anisotropy coefficient or grid size parameter
$\mathbf{J}$	Jacobian matrix
l	Path length
$<l>$	Mean path length
$<l_A>$	Mean amplitude-weighted path length
$\mathbf{L}$	Laplacian regularization matrix
m	Number of start points for each grid search round
n	Refractive index
$r_{x,y,z}$	Rotation angle with respect to the x-, y- or z-axis
$s_{x,y,z}$	Scaling parameter along the x-, y- or z-axis
$t_{x,y,z}$	Translation step along the x-, y- or z-axis
μ_a	Absorption coefficient
μ_s	Scattering coefficient
γ	Weight parameter for landmarks in the surface registration

Software and Toolboxes

iso2mesh	Toolbox for generating triangular surface and tetrahedral volume meshes with Delaunay triangulation [1].
metch	Mesh match toolbox for projecting points to a meshed surface [2].
MCX	Software for GPU-accelerated photon simulations, written in CUDA for Nvidia cards [3].

Contents

Chapter 1

Introduction

Diffuse optical tomography (DOT) images cortical hemodynamic changes, which contain valuable information on brain health and function. Potential applications range from improved detection of seizures to better understanding of affective disorders, such as autism, depression and anxiety. The relatively practical setup is suitable for measuring awake children, which is challenging with the alternative modalities. Furthermore, DOT is not restricted to clinical needs, but enables basic research on healthy brain development, which is of high scientific and societal importance. This thesis presents computational methods for increasing the accuracy of DOT in children.

Compared to functional magnetic resonance imaging (fMRI) or positron emission tomography (PET), DOT is fairly inexpensive, transportable, and does not require special shielded rooms. It also provides higher temporal resolution [4] and enables continuous bedside measurements of even critically injured patients. Moreover, no radiation dose as in PET or loud sounds as in fMRI are involved, and the patient does not have to be isolated or completely stable. Electroencephalography (EEG) also provides a convenient arrangement, but DOT has a higher spatial resolution and better movement-tolerance [4, 5]. Furthermore, EEG measures electrical signals, whereas DOT can image the metabolic and vascular responses to neuronal activity.

An increase in brain activity, for example, due to processing of external stimuli, causes a local dilation of the arterioles, which increases the total hemoglobin concentration (HbT) [4, 6, 7]. In DOT, tissue is illuminated with near-infrared (NIR) light from the wavelength range of 650–950 nm, where hemoglobin is the greatest absorber of light [8], making the detected signal sensitive to changes in its concentration. In DOT difference imaging, the aim is to reconstruct three-dimensional maps of the absorption coefficient changes, which can be directly converted to changes in the HbT.

The near-infrared range opens an optical window into the cerebral cortex, since light can transmit to and reflect back from a few centimeters deep, making DOT best applicable for young subjects with a smaller head and a thinner scalp and skull [9, 10]. The window was discovered already in 1977 [11], but the first three-dimensional DOT images from a neonate subject are from 2002 [12]. DOT has been used in a variety of studies from imaging seizures of a neonate with hypoxic-ischaemic encephalopathy [13] to mapping hemodynamic perturbations on the adult forehead [7], but is not yet in clinical use in Finland. However, DOT is the imaging analog of near-infrared spectroscopy (NIRS) [8], which the common clinical tool pulse-oximeter is based on. NIRS is also increasingly applied in continuous monitoring of cerebral oxygenation.

To realize the potential of DOT in children, this thesis aims to improve the accuracy of modeling light transport in the head, while maintaining the comfortability of the measurements. The work was done in the NIRS group at Aalto University, and the following section will further explain the problem statement.

1.1 Problem statement and structure of the thesis

The forward problem of an imaging modality means estimating the measured signals for a known target and sensor locations [14]. In DOT, this corresponds to modeling light transport, and the problem is solved either numerically from a diffusion equation or statistically with Monte Carlo (MC) methods. Both approaches benefit from a realistic segmented model of the head anatomy along with the baseline tissue-specific optical parameters and the locations of the light sources and detectors, jointly referred to as optodes [9]. This thesis uses the term *optical head model* to refer to these three components.

As was discussed, DOT aims to estimate a realistic three-dimensional distribution of the optical parameter changes that reconstructs the measurements. This corresponds to an inverse problem of light transport. However, the inverse solution always requires one or multiple forward simulations, thus the accuracy of the image depends on the correctness of the optical model. Consequently, the goal of this thesis is to provide improved methods for generating the model, and increase the amount of prior information in the reconstruction to improve the image quality [10, 15, 16]. The methods are especially developed for two-year-olds participating in a study on affective touch, but are applicable to other subjects and age groups as well.

The most accurate methods for obtaining the anatomical model are computed tomography (CT) and magnetic resonance imaging (MR). However, these are impractical for toddlers in most circumstances. Instead, this thesis utilizes an atlas model for two-year-olds, corresponding to the average MR image [17]. To include individual head properties, the template is deformed to match the target head surface reconstructed with photogrammetry. The measurement probe, which contains the optodes, is also photographed. However, only some additional markers are left visible after the probe is attached to the head with a bandage. This thesis presents an interpolation scheme for estimating the locations of the optodes from the visible markers and the known layout of the measurement probe. Since literature does not provide values for the tissue-specific optical parameters in two-year-olds, the work also contains an iterative random search based algorithm for fitting the parameters.

The models obtained are applied to demonstrate the performance of DOT in reconstructing simulated cortical activations. One important benefit of the atlas-based approach is that the individual subjects' results can be deformed back to the common template for comparisons across the subjects [18]. This enables locating the common brain regions that respond to a stimulus in all individuals on average. This type of knowledge is required in surgical treatment planning to preserve important functional areas.

To conclude, this thesis describes a three-step process of computing individually-shaped head models with the optode locations and tissue-specific optical parameters. The topics are handled in this order. Chapter 2 starts by introducing approaches chosen in previous studies, explains our specific needs and justifies the main methodological choices. Chapter 3 continues with presenting the exact algorithms, with some implementation details discussed more in Chapter 4. The performance of the methods is evaluated in Chapter 5, and further discussion on possible improvements and alternative approaches is given in Chapter 6.

Chapter 2

Background for optical models

This master's thesis presents the generation of optical head models for 17 two-year-old subjects. The children participated in a study on affective touch, which is part of the FinnBrain Birth Cohort Study [19]. A similar study was previously conducted on two-month-olds [6].

Affective touch refers to pleasant, gentle and slow stroking with the speed of 3–10 cm/s, which stimulates C-tactile nerve fibers [6, 20]. Lack of affective touch and caressing in the childhood have been reported to affect negatively all aspects of normal neurodevelopment [21]. Thus, it is of clinical relevance to be able to locate the brain regions that respond to affective touch and not to non-affective touch. The developmental trajectories from birth to adulthood are also of interest. Many groups have recently studied affective touch in infants [20], but this thesis contributes to possibly the first study in two-year-olds. The child was sitting on the parent's lap for the approximately 50-minute measurement session, which would be a practically impossible arrangement with fMRI.

In the actual measurement session, the subject was stroked with a soft brush in an affective and a non-affective (fast, discriminative) manner with a measurement probe placed over his/her left frontotemporal brain cortex. The probe is part of our in-house DOT system introduced in [22, 23], which enables overlapping measurements with 15 laser source fibers and 15 detector fiber bundles accompanied with photomultiplier tubes. The device operates in frequency domain and modulates the input light at 100 MHz. We used one input light wavelength of 798 nm and measured modulation amplitude to reconstruct HbT perturbations that result from vascular diameter changes in response to neuronal activation [24]. The following sections of this chapter explain the background for the contributions of this thesis to the study.

2.1 Anatomical head models

All applications of DOT require a model of the target distribution of optical properties. The most accurate ways for obtaining anatomical head models are magnetic resonance imaging (MRI) and computed tomography (CT). However, these approaches are impractical for two-year-olds; the former since it requires stability of the child and being alone, the latter due to the radiation dose. CT images are practically never taken of a healthy subject. If we would acquire the MR images for each subject, we would have to segment each model individually, which always requires some manual work. Consequently, previous literature has introduced a variety of alternatives to replace subject-specific anatomical images. In the following, we assume that only external information on the target head shape is available.

The simplest ways to model the head include infinite homogeneous slabs and semi-infinite homogeneous mediums [25, 26], which can be justified by the fact that the measurement depth is only a few centimeters into the tissue [7]. These geometries also enable solving the forward problem of light propagation analytically [8]. An equally simple approach is to use readily segmented head models or brain atlas templates from the same age group without subject-wise modifications [6]. This can be justified if the head shapes are very alike, but generally it is better to utilize the information on the individual head shape. One approach is to model the correct exterior shape, but with a simplified interior, which can be homogeneous or layered [15, 16]. The former approach was chosen in [12, 27], where a doll-head phantom was warped to match the locations of the sources and detectors on the target head surface. Yet, simulations have shown that homogeneous models produce poorer reconstructed image quality than more accurate anatomical models [10], though layered models might perform more satisfactorily [16]. Nevertheless, a better approach is to warp an anatomically accurate volume image, for example, from another healthy subject of the same age or an averaged model from an atlas. A problem with the former is the amount of subject-specific details included, compared to averaged models [17]. Probably the best approach is to use a probabilistic atlas, where voxel-wise probabilities of each tissue type are given instead of an absolute segmentation [16].

Currently, there exists no probabilistic atlas for two-year-olds, but a normal atlas is provided by Shi et al. in [17]. The atlas is an average of 95 T1-weighted, individually segmented MR images registered to a common reference space with high-quality algorithms [17]. Shi et al. had readily segmented the template into three tissue types: cerebrospinal fluid (CSF), gray matter (GM) and white matter (WM). A group member added the scalp

and skull layer by thresholding the averaged intensity image, producing a $181 \times 217 \times 181$ matrix template with voxel side length of 1 mm.

To obtain the individual anatomical models, the author deformed the template to register it to the head surface for each individual. This approach is called atlas-based DOT, as discussed next. Image registration, or geometric alignment [28], is a common step especially in multi-modal imaging. However, available algorithms are typically meant for registering two images of the same individual, whereas the goal in this thesis is to register a general volume image to the individual target surface.

2.1.1 Atlas-based DOT

The validity of atlas-based DOT has been discussed, for example, in [18], where atlas-based reconstructions of visual evoked responses showed sufficient similarity to fMRI results. Furthermore, the average localization error compared to subject-specific anatomical model reconstructions was 2.7 mm, which is within the error 0.5–1 cm associated with the method with accurate anatomical models [18]. Atlas-based DOT includes the drawbacks that the inner contents of the subject's brain may differ from that of the general model and the insides might not deform with the exterior surface. However, simulations suggests that successful image reconstruction has some tolerance to the accuracy of the inner tissue distribution [16]. Simulations with rigidly transformed templates also suggest that the maximum similarity in GM distribution and sensitivity values to the subject-specific model occurs in the regions that we probed in the affective touch study [29].

To begin with, atlas-based DOT requires a model of the target head surface, to which the template surface is registered. Since we are not using anatomical imaging modalities, a common approach is to present the surface as points measured from it. Possible methods for obtaining the points include the digitizer pen (Polhemus Tracker) [18] and photogrammetry, the latter of which we use. Photogrammetry refers to reconstructing a three-dimensional point from images taken of it from two or more different angles simultaneously. We use two camera angles, which is called stereoscopic imaging. The principal idea is that the view vectors—lines connecting the pinhole camera center and the image of a point—approximately intersect at the target point. The points seen by a camera pair are reconstructed in the coordinate system of either of the cameras. Prior to this the camera pair is calibrated by imaging a calibration object. The two-camera system is placed at multiple locations with respect to the head, and in the end, rigid transformations are used to present all points in the same coordinate frame. A group member implemented the process with a previously developed in-house software.

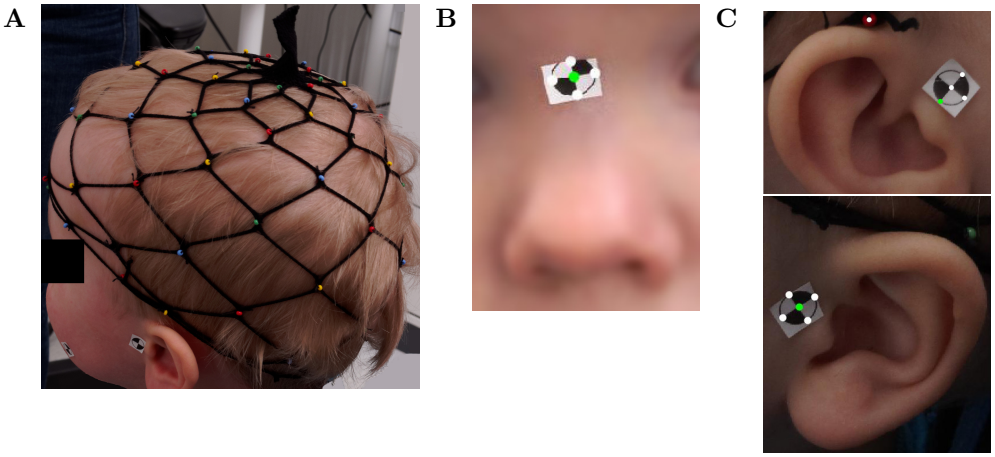

Figure 2.1 *The head shape is defined by the pearl points on the surface* (A)*, the nasion* (B) *and the preauricular points* (C)*.*

The target set, or cranial fiducials, consisted of points on the child's head surface and the three anatomical landmarks. The surface points were marked with colored glass pearls sewn to a stretchable mesh cap shown in Fig 2.1A. The mesh has approximately 70 pearls of which 60 on average were visible in the photographs. The landmarks include the nasion (NAS), and the left (LPA) and right preauricular points (RPA), which were marked with stickers. Nasion is the depression at the root of the nose in Fig. 2.1B [30]. The green preauricular points in Figs. 2.1C and 3.3C lie just in front of the upper end of the tragus [30]. For some subjects, there was inaccuracy in the placement of the stickers, due to movement of the child, long hair and fast pace; we did not want to delay the measurements and frustrate the child at this point so that we could measure actual data as well. Images were taken from 5–7 directions with the mesh and from one direction with the probe with two Olympus E-PL5 cameras with Leica Panasonic 25 mm f/1.4 lenses. The cameras were attached to an aluminium frame to keep their relative positions stable during the measurement.

For the actual deformation, the author decided to apply a non-rigid nine-parameter affine transformation with anisotropic scaling, rotation and translation, performed in this order. The idea is to first make the template the same size and shape as the target head, and then find the matching orientation and location. It is also more reasonable to scale the template in its original orientation where each coordinate axis is normal to two of the anatomical planes (see section 3.1). The parameters include the anisotropic scaling coefficients s_x, s_y and s_z, the rotation angles r_x, r_y and r_z in radians,

and the translation lengths t_x, t_y and t_z in millimeters. All of the transformations can be presented as 4×4 matrices given in the Appendix A. These operate on the homogeneous coordinates of three-dimensional points, which have a fourth dimension corresponding to a scale set to 1.

Rigid affine transformations have more commonly been used in atlas-based DOT [29, 31, 32], but anisotropic scaling was added to enable modifying the template shape. The author noticed the need for this when comparing the results according to different combinations of the transformation parameters. Though even more advanced methods exist, the complexity and workload of the chosen approach was in balance with the resolution of the segmented template, and especially the accuracy of the head surface as given by the limited number of pearls. Non-linear free-form (elastic) deformations, though generally more accurate [18, 33], would probably attempt to model variations in the fit of the mesh, and require more target points or some information on the internal structure of the target head, which we did not have [29]. Furthermore, though elastic deformations are superior in regions that exhibit high curvature [18], our probed region is relatively flat. Finally, affine transformations are easy to invert, which was required for spatial normalization, meaning co-registering individual results to the common atlas template for group-level analysis and visualization [17, 18].

2.2 Completing the optical model

In addition to the segmented anatomical model, the forward problem solution requires the locations of the light optodes and the optical parameters of the tissue types. We start with the former, since accurate optode locations are essential for reliable estimation of the parameters [12], and also for the positional correctness of reconstructed difference images [9].

2.2.1 Probe placement

The high-density fiber-optic probe in Fig. 2.2A establishes the connection between the subject and the instrument. The flexible probe is capable to match individual head shapes in the probed region independent of subject age. The prism terminals of the 15 source fibers and 15 detector fiber bundles have been embedded to a silicone-based (Accutrans Black, Ultronics/Coltène) bendable and flat platform, which is connected to the main instrument by the optical fibers. The dimensions of the probe are approximately $14\,\text{cm} \times 10\,\text{cm}$ and the optode layout is visualized in Fig. 2.2B. An accelerometer is also attached to the lower right corner for detecting subject movement.

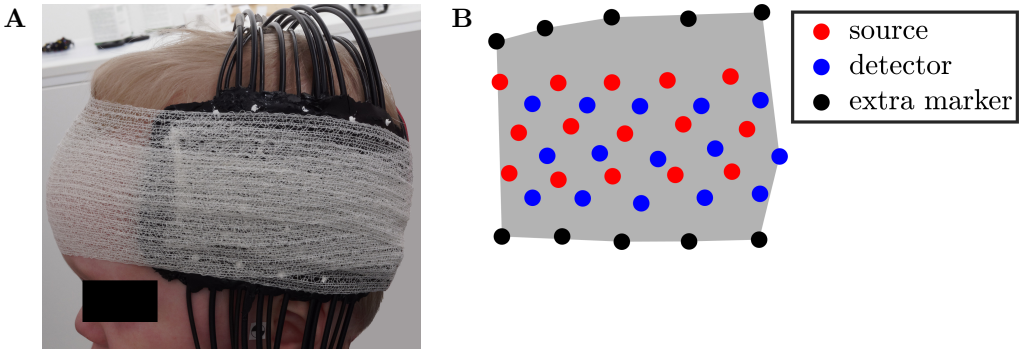

Figure 2.2 *The probe on the frontotemporal cortex* (A) *and the flat probe optode layout* (B).

The probe is attached by wrapping self-adhesive bandage around the head while holding the probe in place (see Fig. 2.2A). A tight wrap is needed to prevent light leakage between the most distant source–detector pairs, which enable the most deep measurements [25]. The problem is that multiple layers of the white bandage are not transparent, thus wrapping hides most of the optode markers. This prevents reconstructing their locations directly with photogrammetry. Yet, some of the ten extra markers on the edges of the probe are visible, and we can reconstruct their positions with respect to the landmarks. In this thesis, the locations of the optodes are interpolated based on these markers and the known flat geometry of the probe (see Fig. 2.2B).

The described problem of interpolating hidden optodes seems to be relatively specific to our group: Many others have wearable headgear with the optodes visible on the outer surface. Alternatively, Bluestone et al. reconstructed the locations from the marks that the optodes had pressed on hairless skin, but this would be ethically problematic with infants [7]. A better approach is to use the marks left to a custom-built headgear [12]. On the other hand, many have preferred not to use photogrammetry (or Polhemus) since it requires stability from the child [5]. One option is to place the optodes to a flexible head cap according to a known coordinate system, such as a subset of the 10-5 points [13], so that the anatomical model and the landmarks are sufficient to reconstruct the optode layout on the surface—with limited precision. The landmarks can also be located by measuring the head circumference along with lateral and central semi-circumferences between the landmarks [5, 20]. Lloyd-Fox et al. combined this with photographs (not photogrammetry) to estimate the location of the probe with respect to the landmarks. Then they projected the fixed geometry of the source-detector array onto the head surface [5]. This thesis implements a similar idea for obtaining the initial guesses for the interpolation (see section 3.3.1).

2.2.2 Optical parameters

The optical parameters are the final essential part of the forward solution since they determine the propagation of light in the tissue. In simulations, the wavelength-dependent parameters are used to indirectly select the wavelength of the input light. Inaccurate parameters reduce the spatial accuracy and contrast of reconstructed images [10]. Furthermore, in practice, we have observed that the results can be very sensitive to the parameters.

Photons and tissue mainly interact via elastic scattering. Consequently, photon trajectories are controlled by the scattering coefficients μ_s, though the amount of detected light also depends on the absorption coefficients μ_a. Both μ_a and μ_s are defined as the reciprocals of typical distances that a photon travels before it is absorbed or scattered, respectively [25]. Several properties of the trajectories, such as the scattering directions, propagation speeds and reflections at tissue boundaries depend also on the refractive index n and the anisotropy coefficient g. However, this thesis focuses on μ_a and μ_s which vary the most for different tissue types (see for example [9, 34, 35]). Responses to stimuli are also assumed to show in these parameters, especially as changes in the absorption coefficient which is the most sensitive to the physiological processes in the tissue [10, 15, 36, 37].

Despite the importance of the parameters in optical imaging, surprisingly little literature exists on their in vivo values at different ages [35]. Above all, we found no published parameters of the two-year-old brain. However, Fukui et al. have reported values for neonates and adults at almost the correct wavelength of 800 nm (our measurements were at 798 nm) [38]. The author decided to use them as the basis for selecting the parameters and their standard deviations (std, which will be needed in section 3.4.1), given in Table 2.1.

Tissue type	μ_a mean $\pm$ std [mm^{-1}]	μ_s mean $\pm$ std [mm^{-1}]	g	n
Air	0	0	1	1
Scalp and skull	0.016 ± 0.001	16 ± 1.5	0.9	1.4
CSF	0.004	0.3	0.9	1.4
GM	0.042 ± 0.003	13.5 ± 4.25	0.9	1.4
WM	0.0255 ± 0.0058	50.5 ± 20.25	0.9	1.4

Table 2.1: *Optical parameters for each tissue type in the segmented model.*

For GM and WM, the values are simply the average of the neonatal and adult parameters. These were the only parameters that Fukui et al. reported to change from birth to adulthood and reflect the development of the brain. Though Fukui et al. separated the scalp and skull parameters, here the skull

values present the combination, since these are closer to the values used in [6] with wavelengths of 758 nm and 824 nm. The scattering coefficient of CSF is as in [6, 39]. Yet, simulations have shown that due to the irregularity of the CSF layer, all values below $3\,\mathrm{mm}^{-1}$ can be used with little change in the detected signal (at least with source–detector distances (SDD) under 40 mm; g might need to be modified) [10, 40]. The value for n is as in [8, 38], and the value for g is based on [35, 37] so that the reduced scattering coefficients $\mu_s^{'} = (1-g)\mu_s$ match the values tabulated in [38].

Several concerns are related to the used literature values: Most values were measured in vitro—from dead tissue separated from the human—and the table given in [41] suggests huge variations between in vitro and in vivo values. There also appear to be differences in values according to different sources, especially for GM and WM [35]. In addition, the chosen approach of averaging adult and neonatal GM and WM parameters has no theoretical basis. At first, the idea that development would be half-way seems inconsistent with the amount of learning that happens after the age of two. However, the moment of birth is a very extreme point for the comparison, and the brain rate of growth and development is dramatic during the first year compared to any other period in life [17, 42]. In fact, white matter myelination processes to adult-like patterns by the age of two, and the brain volume increases from 50 to 90% of the adult volume by the age of three [17]. A medical doctor was consulted and he considered averaging a justified approach.

Accurate estimation of the optical parameters is undoubtedly a very challenging task. Measurements should be made in vivo, which introduces several instrumental and practical challenges: The DOT device must measure time resolved parameters, not just intensity. Obtaining correctly calibrated absolute data is demanding. The depth sensitivity of DOT is limited to a few centimeters, which complicates the estimation of white matter parameters especially after early childhood [38]. Furthermore, the computation is challenging since we have a multi-parameter optimization problem which requires a very accurate optical model of the head.

The scientific and clinical community would greatly benefit from more accurate optical parameters for two-year-olds and other specific age groups. This would improve the accuracy of DOT and enable distinguishing between healthy and pathological tissue. Our instrument fulfills the requirements for estimation: data calibration is enabled along with time-resolved measurements of phase since the FD system inputs light as a frequency modulated (sinusoidal) wave [8, 15]. To initialize this process, this thesis presents an algorithm that searches for the correct parameters by comparing simulated and reference data. Since correctly calibrated absolute data was not available for this thesis, estimates from real data can not be presented.

Chapter 3

Methods

To begin with, we have the segmented anatomical template, the coordinates of the three landmarks from the target and the template, a set of points from the target head surface and the uncovered regions of the probe, and initial guesses for the optical parameters, as discussed in chapter 2. The ultimate end goal is a correctly shaped anatomical model with the locations of the optodes and better estimates for the optical parameters. This chapter explains the methods developed for these three tasks, and ends with an example of applying the completed model in DOT difference imaging. The first section introduces the initial preparations on the target point sets and presents the working coordinate frame. From this chapter on, unless stated otherwise, all work was performed by the author.

3.1 Initial data preparations

Prior to the model generation steps of this thesis, photogrammetry has been used to reconstruct the locations of the visible probe points, head surface points, landmarks and facial sticker points. The latter mainly contains points selected from the landmark stickers since others were below the template which only extends below the nose. All points are given in the coordinate system of one of the cameras at one camera position and orientation. As an initial registration step, we use landmarks to present the points in the template's coordinate frame. The algorithm for this was modified from a previous in-house version. The landmarks on the template were manually selected by a medical doctor.

In the head coordinate system according to the landmarks, the x-axis points from LPA to RPA and the origin is at the orthogonal intersection of x-axis and a line from the nasion towards the axis. The direction of the

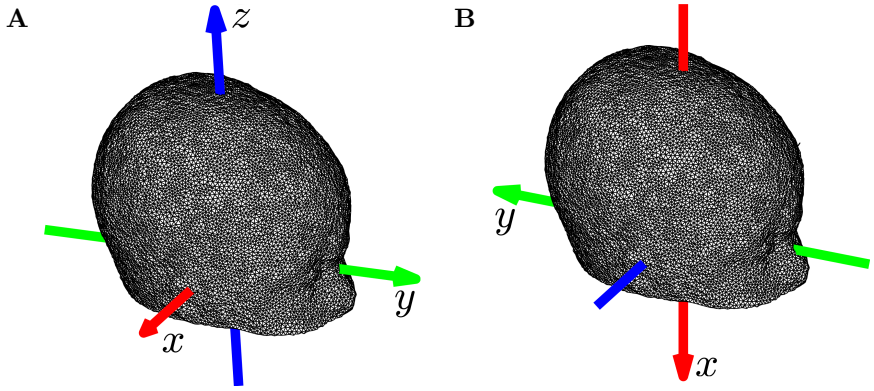

Figure 3.1 *The coordinate system for the initial registration step* (A) *and of the template* (B).

y-axis is from the origin to the nasion, and the z-axis direction is according to the cross product of the two defined axes, running from the inferior to the superior part of the head. The frame is presented in Fig. 3.1A. This is the common approach for determining the head system when only external information is available, as in most functional imaging systems [43]. For the initial registration step, the algorithm first defines the head system origin and axes according to the subject's landmarks and those of the template. Then it calculates the coordinates of the points according to the subject system, and uses them to present the points in the template's coordinate system. This works well if the anatomical placements of the landmarks match.

In the template's coordinate system, the origin is at the upper left corner of the image and the axes are defined by the sagittal, coronal and horizontal planes. The x-axis is superior to inferior, y-axis anterior to posterior, and z-axis is from right to left. In the original downloaded version [17], the template is in the Talairach (also MNI or Stereotaxic) coordinate system, but a group member rotated the axes at an early image processing step. During the optimization process, transformations are performed in the template coordinate system, but the origin is moved to the center of the head system as shown in Fig. 3.1B. With this choice, rotations and scaling are performed with respect to the center of the head. Choosing an appropriate coordinate frame is an important step prior to the optimization of the affine parameters.

After the initial registration, we replaced possible multiple reconstructions of a point with their average; different camera pairs do not reconstruct the exact same coordinates, especially now that the image points have been selected manually. The benefits of the averaging are that it speeds up the computation since we have fewer target points to consider, and the weight of a point doesn't depend on the number of cameras that have seen the point.

We continued with dropping the pearl points radially to compensate for the height of the pearl and the thickness of the net. The distance from the head surface to the center of the pearl, which was the target in the image, was measured to be 1.5 mm. To find the radial direction, we fit a sphere to the surface points, and used its center as the end point of the radial direction. We estimated the head center as the least squares solution to the difference between the sphere radius and the distances from the target points to the head center. We used two of MATLAB's numerical minimization tools, fminsearch and lsqnonlin, and chose the answer with the smaller final value of the cost function. Since the subjects were two-year-old, they had some hair lifting the mesh from the scalp. One approach would be to estimate the lift and add it to the radial drop, but the estimation would be rather difficult. Moreover, we observed that even for children with relatively lot of hair, the mesh is rather tight and hair is pushed through the holes in the net. Three of the subjects also had braids which was observed beneficial in the sense that they collected hair away from most regions enabling skin-contact.

Braids of course caused outliers to the pearl set, and sometimes the hair had gathered at the top lifting the mesh. Luckily, it was rather easy to identify points clearly lifted by hair or otherwise erroneous from the photographs. As the final data preparation step, we manually removed the outliers, or a part of the points in a problematic region to remove the weight of the area. We removed on average two points (range 0–5), and in the end we had on average 60 (standard deviation (std) 8, range 34–69) pearl points and 16 (std 4, range 8–25) facial sticker points to guide the model deformation.

3.2 Model deformation

The main task in the model deformation is to find the nine parameters of the affine transformation that matches the template surface to the set of points from the target surface. We recall that the parameters include the anisotropic scaling coefficients s_x, s_y and s_z, the rotation angles r_x, r_y and r_z in radians, and the translation lengths t_x, t_y and t_z in millimeters. We chose to modify the approach from [33], with the key idea to present the template surface as a triangular mesh and minimize the distance from the target points to this mesh [28]. This is called surface-based registration. We tested different combinations of the parameters and searched for the one that minimizes a chosen cost, or objective, function. For this, we implemented a parameter grid search algorithm as in [28].

We used the iso2mesh toolbox [1, 44] for generating the triangular surface meshes for the templates. The software performs a Delaunay triangulation.

During the iterative optimization process we modify the mesh, not the template, which is a valid approach since the deformed mesh and the mesh of the deformed template were observed to match sufficiently. Furthermore, this approach is beneficial since it is more faster to transform just the nodes of the original mesh versus deforming the template and re-meshing it for each parameter trial set. The latter approach would be practically impossible. Above all, the mesh forms a continuous presentation of the surface compared to the voxel model, though in principle we could just minimize the distances to closest surface voxel. Meshes have also been utilized by others [18, 29].

Another important factor in the computational efficiency and accuracy is finding the shortest distance from a target point to the mesh. Intuitively, the closest point must be either at a node (vertex), on a line segment between two nodes (edge) or then inside a triangle. This is implemented in the point2trimesh-function written by Daniel Frisch [45]. The key steps in the source code are:

1. Find the closest vertex.

2. Find those line segments, for which the closest point to the query point on the corresponding line is within the segment. In other words, the perpendicular intersection from the query point to the line must be within the edge. Find the closest point from these intersections.

3. Find those triangles, for which the closest point on the corresponding plane is inside the triangle. The perpendicular intersection is computed by subtracting from the query point, the projection of the vector between the query point and one of the nodes along the normal direction of the triangle. Barycentric coordinates determine whether this point is inside the triangle. From the one that are, find the closest.

4. From the three previous results, select the ultimate closest point.

Due to observed excellent performance and limited time resources, we decided to utilize the function, yet plan to write our own in the future. Simpler approaches are also available, such as the one provided in the metch toolbox [2]; the function finds the closest node, and returns the length of the segment between the query point and the node projected to the normal direction of the node. Yet, we preferred the more accurate method, especially since the mesh has a limited density. Furthermore, we did not observe major differences in their computation times, especially since point2trimesh enables parallel handling of query points for increased speed.

3.2.1 Parameter grid search algorithm

The implemented parameter grid search algorithm was presented in [28] and also used in [33]. The idea is that the search space is a nine-dimensional grid with one dimension per parameter. For each parameter p_i, the one-dimensional discrete search range is formed by g values on both sides of the initial guess $p_{i,0}$ with a step length of d_i. Consequently, there are $(2g+1)$ options for each parameter, and the search space is formed by all $(2g+1)^9$ possible combinations. The cost function (see section 3.2.2) is evaluated at each grid location, and for the next iteration, denser grids are formed around the m best combinations. Thus, the search space is controlled by the positive integers g and m and real numbers d_i. The exact iteration steps are as follows:

0. Form the initial search grid by selecting the initial parameter vector, g, m and d_i, $i = 1$–9. See section 4.1 and 4.1.2.

1. Calculate the cost function value at each grid point in parallel. Save m best combinations.

2. Divide each d_i by 2. Create new search grids around the m best combinations from the previous step.

3. Calculate cost function values in parallel for each combination from all m grids. Save m ultimately best combinations.

4. If the improvement in cost is less than a chosen limit ϵ, but not the same as the starting value, or the maximum number of iterations has been reached, stop the iteration. Otherwise, go to step 2.

The final result is the best of the m results from the last iteration. Fig. 3.2 visualizes the grid update step for the choices $g = 1$ and $m = 2$ with $i = 2$ for simplicity. The benefits of the algorithm include that it is easy to control the search range of the parameters and follow the progress of the optimization. Yet, the method suffers from *the curse of dimensionality*, as will be discussed in section 4.1.2 along with other details on the implementation.

3.2.2 Cost function

The first attempt was to use the same cost function as in [33]. The function combines surface- and point-based registration via a weighted sum as

$$\text{cost}_{\text{original}} = \text{SRE} + \gamma \text{LRE}, \tag{3.1}$$

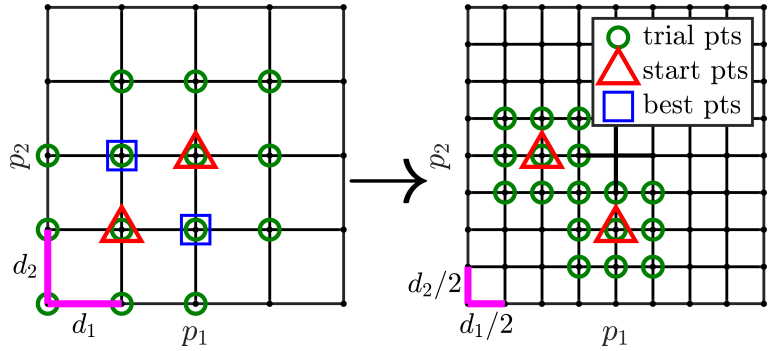

Figure 3.2 *Grid search and following grid update for two parameters. The search space in the dense grid is formed around the optimums from the sparse grid. ("Points" is shortened as "pts".)*

where SRE stands for surface registration error and LRE for landmark registration error. SRE is calculated as the average shortest distance from the target head surface points (excluding landmarks) to the mesh, and LRE is the mean Euclidean distance between corresponding template and target landmarks. The weight parameter γ is typically in the range 1–1.4, yet the optimal value is case-dependent [33]. Nevertheless, a relatively heavy weight is put on the exact match of the landmarks. For this to make sense, the landmarks should be chosen at the exact same anatomical locations, which is generally not the case: The template landmarks were selected by hand from the MR-images, which is challenging. Since the atlas is an averaged model, the anatomical locations and dimensions might not be fully realistic. Moreover, the doctor reported that he aimed to select the preauricular points as the red point in Fig. 3.3C, instead of the green point which is closer to the target of the stickers. Thus, for all subjects, LPA and RPA are at least in front of and slightly inferior to their references on the template. Yet, the subject landmark placements also differ from the aimed locations. Especially the preauricular points have been clearly misplaced for some of the children, for example due to hair being in the way as in Fig. 3.3D or the child moving the stickers. RPA and LPA are generally difficult to locate correctly or symmetrically.

The inaccuracies in the placement of the landmarks cause absolute orientation errors between the template and the target heads in the initial registration step. As a result, the initial match of target and template landmarks is rather good, but pearl points are clearly detached from the template surface. We observed that the LRE term in the cost function in Eq. 3.1 amplified the orientation errors, and mostly prevented rigid transformations since these would have misplaced the landmarks with respect to each other. The tem-

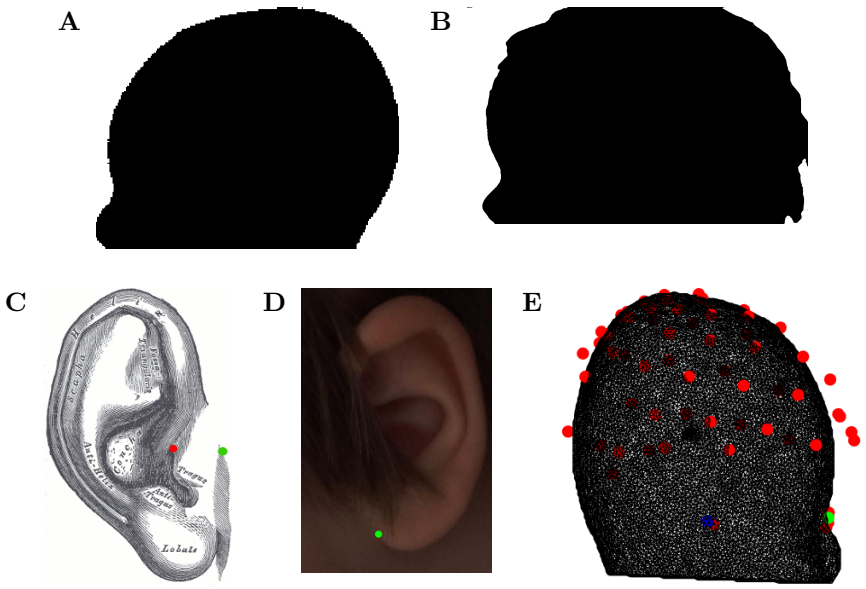

Figure 3.3 *The nasion curvature varies between the template* (A) *and the subject* (B). *The template preauricular is at the red point, whereas stickers are closer to the green* (C*; reprinted from* [46]) *or worse* (D). *Misplacements cause bad head shapes compared to the red pearls if we minimize LRE* (E).

plate was mainly scaled to reach the target surface points, which resulted in unrealistic head shapes and poor matching along axial slices as demonstrated in Fig. 3.3E (start situation in Fig. 5.3). All in all, though it is understandable that limited time was put into placing the physical stickers on the two-year-olds, the inaccuracies prevented us from applying the cost function in Eq. 3.1. The only solution was to loosen the landmark registration requirements by removing LRE from the cost, as described next. We will return to the initial absolute orientation errors and fixing them with rigid transformations in section 4.1.1.

The second attempt for the cost function was to leave out the point-wise registration and minimize just the SRE for all target points, including the landmarks. This worked well for three of the subjects, but for the others, problems occurred due to differences in the y-directional depths of the nasions: It seems that the template has a less depressed nasion region than our subjects, as can be observed by comparing the side profiles in Fig 3.3A and Fig 3.3B. Furthermore, looking carefully at the template mesh, the nasion seems to be located on a bump instead of the deepest location. All in all, the target nasion was often deeper than the template nasion would have predicted. To fix this, the algorithm was observed to rotate the template to

match the target nasion with deeper parts on the side of the nose. Since the models were also scaled narrower to match the target nasion, they did not reach all surface points.

Based on the previous observations, the final conclusion was to handle the nasion separately for the 14 subjects for whom the previous approach was not ideal. Instead of including the nasion into the target set of the SRE, we developed a new point-wise nasion separation term with a weight factor of 1/16, chosen to match the magnitude of the SRE. The new term has separate components for coronal/frontal plane separation and depth separation, which include a tolerance of 4 mm for the former, and of 6 or 12 mm for the latter separation, to account for inaccuracies in the placement of the nasion sticker and observed anatomical differences in the depth of the nasion. The tolerance limits were based on observing the images and trial-and-error, however, in practice the tolerances acted as upper bounds that the final separations did not exceed. The 12 mm depth tolerance seems high, but looks very realistic and produces a good fit especially in the probed region of the head surface.

To summarize, the general form of the built cost function is

$$\begin{aligned} \text{cost} = \alpha\Big[\text{SRE}_{\text{all}}\Big] + (1-\alpha)\Big[\text{SRE}_{\text{all}\setminus\text{NAS}} \;+\; \max(\gamma_1,\, \gamma_2)\text{NRE}_{x,z} \\ + \gamma_1\text{NRE}_{y,1} \;+\; \gamma_2\text{NRE}_{y,2}\Big], \end{aligned} \tag{3.2}$$

where NRE is an acronym for nasion registration error. $\text{NRE}_{x,z}$ refers to the coronal plane separation, and $\text{NRE}_{y,1}$ and $\text{NRE}_{y,2}$ to the depth separation for the two alternative thresholds. The three possible weight parameter combinations include

$$\begin{cases} \alpha = 1, \\ \alpha = 0,\ \gamma_1 = 1/16,\ \gamma_2 = 0, \\ \alpha = 0,\ \gamma_1 = 0,\ \gamma_2 = 1/16. \end{cases}$$

For each subject, the chosen cost is the combination that produced the best results. If one cost had to be picked for all subjects, we would suggest using either of the versions with separate NRE—they worked satisfactorily for all subjects. The benefit of NRE is that it guides the template to the correct orientation and height if the mesh has been loose from the top, for example. Generally, the landmarks are not prone to mesh fit related errors.

To conclude, the cost function as in [33] was not ideal since there are inaccuracies in the placements of the landmarks and anatomical differences in the curvature of the nasion. Furthermore, the LRE term prevented from fixing absolute orientation errors and instead rather amplified them. A modified cost function was needed to address these problems. However, we still

have to encourage the rotations that can fix axis orientation errors: If you rotate the template with respect to its center, this detaches especially the landmarks from the surface, which is not desirable. Thus, we decided to change the center of rotation to the nasion, which is usually selected rather accurately (except for the depth differences which can be accounted for with simple translations). This was achieved by adding a translation to match the modified template nasion with the target nasion after the rotations.

To summarize, the affine transformation starts with anisotropic scaling, then the template is rotated with respect to its center, followed by matching the template nasion with the target nasion, and finally translations are performed. A grid search is performed to find the optimal parameters for each step by minimizing the cost function according to Eq. 3.2. Yet, successful registration of the template to the target points also improves the match of the visible probe points with the surface. The next section introduces the algorithm that was developed to estimate the locations of the optodes on the deformed surface.

3.3 Optode localization

We recall from section 2.2.1 that most of the optodes are hidden under the bandage as shown in Fig. 2.2A. Typically, only some of the extra markers on the upper and lower edges in Fig. 2.2B are visible. Furthermore, all visible points are from the outer surface of the probe, whereas our end goal is to deduce the locations of the optodes on the head surface. The starting point for the estimation are the visible points in the template's coordinate system, the deformed template and the known geometry of the flat probe. We assume minimum three initially visible points, of which two are neighbors and all are not from the same line of markers (top or bottom). The algorithm was programmed by modifying a previously developed in-house code. The following text will highlight the approaches that were adapted from the previous version, but most of the actual code was replaced to improve the implementation.

One of the key ideas that we kept was the usage of spherical coordinates to present the locations of the optodes during the optimization phase: We can not move the optodes along the head surface during the search, but since the head region under the probe is usually just slightly curved, a carefully fitted sphere works as an appropriate search surface during the optimization. At each trial point, the spherical coordinates are converted to points on the head surface mesh, thus the goodness of the coordinates is evaluated on the head, as will be described in section 3.3.2. Furthermore, each location can

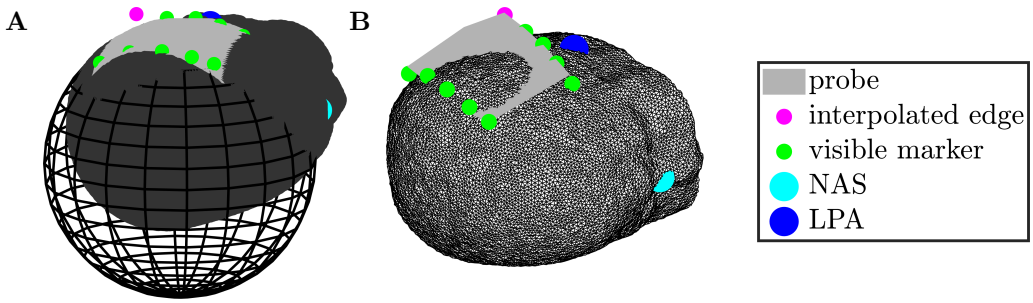

Figure 3.4 *A fitted sphere models the probe surface during fiber interpolation* (A)*, whereas a fitted plane demonstrates the probe before pressed against the head* (B)*.*

be presented with two angles instead of three Cartesian coordinates which simplifies the optimization.

Consequently, the first step in the algorithm is to fit a sphere to the superficial head voxels under the probe. The fit is obtained with the same least squares algorithm that was used for dropping the pearls in section 3.1. Prior to this, we need to define the target voxels, specifically the x-, y- and z-limits for points in the probe region (we recall the template's coordinate system in Fig. 3.1B). The latter depends on the probe width and curvature, whereas the first two determine the extent of the probe as given by the edges of the probe. If an edge has not been reconstructed with photogrammetry, the program interpolates its location using:

- the average direction between visible row-wise neighboring markers;
- the distance on the flat probe from the missing edge to the closest visible point on the same row; and
- a separation scaler determined as the ratio of distances (neighbor separations) in the reconstructed set versus on the flat grid.

The missing edge is interpolated by multiplying the distance on the flat probe with the scaler, and moving this length from the closest visible point along the average direction towards the edge. With the scaler, we account for the curvature of the head and try to avoid stretching the probe region too much. Probe limits are then obtained as the most extreme x- and y-values from all reconstructed and interpolated probe points. The obtained probe dimensions are compared to the known flat dimensions. An example of a fitted sphere along with an interpolated edge is shown in Fig. 3.4A.

The final preparation step accounts for the thickness of the probe which was measured to be approximately 7 mm: When pressed against the head, the

probe bends so that optode locations on the outer surface are further away from each other, and locations on the inner surface are closer to each other than in the flat probe. We approximated that locations along the middle layer of the probe are roughly equally separated as in the flat grid. Since the algorithm will eventually minimize the difference between optode separations in the grid and on the head surface, we have to increase the radius of the fitted sphere and the head size by the probe half-width. Specifically, we scale the template radially using the center of the fitted sphere as the origin. This models the increase in the probe region best and matches the scaling of the fitted sphere radius. Optimization from this on is performed along the scaled surfaces.

3.3.1 Initial guesses for optode locations

The optimization requires initial guesses for all probe points, especially the invisible ones, on the scaled head surface. We know that the initially flat probe is first brought close to the head and then pressed against the surface. This process was modeled to obtain the initial estimates: First, the algorithm uses the visible probe points to estimate the location and position of the flat probe before it is pressed against the head. Then the grid points are projected radially to the scaled head surface using the fitted sphere center. Yet, the initial guesses for the visible points are computed simply as the radial projections of their original reconstructions.

The position and location of the flat grid before it is pressed against the head is obtained with a rigid transformation (rotation and translation) of the grid to the set of visible markers. Since the grid is two-dimensional, we set the z-coordinate for each point as the mean of the visible markers. To simplify the estimation of the transformation, we first fit a plane to the visible points and project the points to this plane. The three-dimensional plane coefficients are solved with MATLAB's backslash operator in the least squares sense. For subjects with under eight seen points, we aid the plane fitting by including the interpolated edge points which were used to define the probe region (see previous section). The benefit of the edge points is that they are far away from each other and guide the fitted plane to a reasonable orientation. Fig. 3.4B gives an example of a fitted plane that is partly inside the head since the markers are already on the surface. Thus, we model the process as if the probe was brought from inside of the head, but this is irrelevant for the end result. All in all, the plane fitting is a critical part of the success of the initial guess, since the transformation between the flat grid and the fitted plane is relatively straightforward to compute.

The fitted plane is further utilized as an interpolation platform for obtain-

ing more target points to guide the estimation of the rigid transformation: If we have fewer than three visible markers from either edge of the probe, we interpolate the two neighboring markers of each visible one. Interpolation follows the idea that was used for the edges, except that now we can use the flat grid distances since we are interpolating on a plane. The rationale for the threshold of three points is that if we have only two points, the rigid transformation might flip the probe grid so that it runs between these points.

Finally, we use Horn's quaternion-based algorithm, implemented by Matt J. [47], to calculate the rigid transformation between the flat grid points (with the chosen z-coordinate) and their corresponding points on the fitted plane. We transform the grid points which correspond to invisible probe points, and drop the points radially to the scaled surface. Lastly, we convert all points into spherical coordinates according to the fitted sphere. Now we have the initial guesses for all optodes and probe markers and we can continue to actual iterative optimization, as discussed next.

3.3.2 Optimizing point-wise separations along the surface mesh

The final estimates for the optode locations in spherical coordinates are obtained by minimizing an objective function that combines the prior knowledge of the probe geometry and the visible markers with the initial guesses for the locations. The qualitative contents of the cost function were adapted from the previous version of the algorithm, and formulated into a weighted sum of three mean squared error (MSE) as

$$\mathrm{cost}_{\mathrm{probe}} = 20\,\mathrm{MSE}_{\mathrm{grid\,sep}} + 10\,\mathrm{MSE}_{\mathrm{visible}} + \mathrm{MSE}_{\mathrm{invisible}}. \tag{3.3}$$

The first error term considers the differences between grid point separations on the flat grid versus on the scaled head surface. We assume that the probe bends to match the head surface so that separations on grid and along the head are comparable. For each grid point, the 25 nearest neighbors on the flat grid are included. The second and third error terms restrict the Euclidean distance from a visible and an invisible, respectively, probe point to its initial guess. The weight factors were chosen empirically, with the idea to emphasize the photogrammetry points since they contain all the initial information that we have on the probe location. The cost function is minimized with MATLAB's fminsearch-function that implements the Nelder-Mead simplex algorithm [48]. First, only the invisible probe points are considered as variables for one fminsearch call with maximum of 400 function evaluations. Then we free all the probe points. Execution stops after 2400 function calls

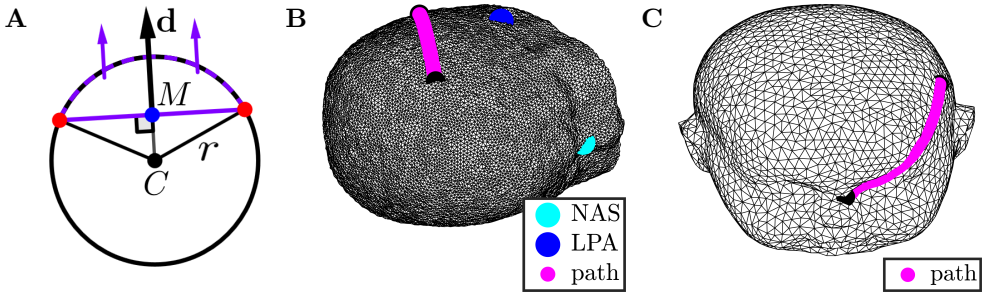

Figure 3.5 *Modeling the head surface as a sphere* (A)*, the line segment (violet) between two points (red) is pulled perpendicularly through the surface to the direction* **d**. *C, r and M mark the center and radius of the sphere, and the middle point of the segment, respectively. Examples of the projected path are given on a subject* (B) *and a doll* (C) *head mesh.*

or when the relative improvement in cost value over two iterations is less than 5%.

The first error term $\mathrm{MSE}_{\mathrm{grid\,sep}}$ requires an algorithm for finding the distance between two points along the head surface. We decided to utilize the triangular surface mesh to present the surface, and compute the distance along the mesh. As for the model registration in section 3.2, we used the iso2mesh toolbox for generating the meshes, but with the Delaunay radius maximum set to 3 mm. To begin with, the algorithm converts the two points into Cartesian coordinates and projects them radially to the scaled surface using the center of the fitted sphere. Next, it selects a dense set of points from the straight line connecting the two points, and projects these points to the surface. The idea is to pull the straight path through the surface and use the intersection curve as the path along the surface. The pull direction is chosen to point from the center of the fitted sphere towards the middle point of the line segment, as visualized in Fig 3.5A. This direction is perpendicular to the line segment. For projecting points to the mesh, we modified a function provided in the metch toolbox [2]. Finally, the distance along the mesh is approximated as the sum of the Euclidean distances between subsequent projected points. Two examples of paths are shown in Fig. 3.5B and 3.5C. The first one connects two probe points on one of the subjects, the latter is on a doll head. The doll model was extracted from CT images taken by medical physicist, Dr. Touko Kaasalainen. It takes approximately 0.008 s to measure a path with 101 line points.

After the optimization, all obtained optode locations are converted into Cartesian coordinates and projected radially to the actual deformed head surface. In addition, the light input directions for each source are computed

as pointing toward the center of the fitted sphere. These are needed for inputting light into the head in the following section 3.4. Generally, the algorithm could use the facial normals of the triangular elements for determining projection and inward directions instead of the radial direction towards the fitted sphere. Yet, since the sphere fits the probe region rather exactly and the drop distances are small, this probably has a negligible effect. Nevertheless, this will be further discussed in chapter 6.

3.4 Applying optical models in DOT

The previous two sections have established the frames of our optical model: We now have the segmented anatomical models and locations of the optodes for each child. These form the contribution of this thesis to the affective touch study introduced in chapter 2. We complete the models by assigning to each tissue type the corresponding optical parameter value according to Table 2.1. In the following section, we introduce an algorithm that could be used to estimate more accurate values for the parameters. The last section describes the image reconstruction algorithm that was also applied in the affective touch study.

Optical parameter estimation is based on multiple forward solutions, as described next. To be able to solve the forward problem, we need to select a model for light propagation, which can be analytical, numerical or statistical. In this thesis, we used statistical Monte Carlo methods implemented by the Monte Carlo eXtreme (MCX) software, which is introduced in section 4.2. Monte Carlo is considered the gold standard method for solving the forward problem since it implements the radiative transfer equation (RTE).

3.4.1 Estimation of optical parameters

The goal in this section is to obtain more accurate estimates for the absorption and scattering coefficients of the scalp and skull, GM and WM tissue types. CSF is excluded from the search in this thesis mainly for simplicity. In addition, as was mentioned earlier, the scattering coefficient of CSF is not expected to significantly affect the measured values [10, 40] and the absorption is relatively small. The three other tissue types probably also change more from birth to adulthood. Furthermore, many current literature values are based on assuming that CSF is pure water or other clear liquid, thus it can perhaps be measured in vitro. Yet, this assumption does not model the veins and connective tissue affecting the scattering and absorption properties of CSF. Thus, CSF should eventually be included in the estimation.

We selected the iterative approach for parameter estimation, meaning that we solve the forward problem for different absorption and scattering parameter combinations and search for the set that best corresponds to the reference data. Methodologically this involves four important points for consideration: how to 1) solve the forward problem accurately and efficiently, 2) sample the parameter space, 3) measure the match between the forward solution and the reference, and 4) evaluate the accuracy of the resulting parameter vector. The first issue has been the topic of this chapter so far. Next, we consider the three other points.

One solution of the forward problem for a single source takes approximately 2.5 min, which corresponds to over 30 min for all 15 sources. Though we can run simulations for multiple tissue parameter sets simultaneously, this unavoidably limits the sample size and demands efficient sampling. Parameter grid search, which was used for model deformation in section 3.2.1, suffers from the curse of dimensionality that would cause major problems with the computation time: To test three values for each parameter, meaning 729 simulations, would take over 18 h with 20 simultaneously running jobs. Thus, instead of the grid search, we decided to perform random search [49] where the values are randomly sampled from a Gaussian distribution for each parameter. Now with 729 simulations we can test 729 different values for each parameter instead of three. Random sampling, as grid search, is a typical hyperparameter optimization method in machine learning [49].

For sampling, we had to select the means and standard deviations for the distributions of each parameter. This was challenging, since we are not sure how far the in vitro values are from in vivo ones, how much do the parameters vary even in resting state and how sensitive our simulated measurements are to the parameters. For simplicity, we decided to assume that the ranges according to [38] are accurate, and the true values lie between the neonatal and adult parameters. For each parameter, we set the mean as the average of the values, and the standard deviation so that four times the chosen value corresponds to the range from neonatal to adult value. This way, the sampled value is in the range with the probability of 95%, thus we leave a small chance for values outside the range. For the scalp and skull layer, the deviation was chosen according to the range between the individual scalp and skull values, since the reported values are the same for neonates and adults. The means and standard deviations were given in Table 2.1. Negative sampled values are replaced with their absolute value, which tilts the distribution towards positive values.

Next we had to choose the measurables for comparing the forward solutions with reference data. Our FD system measures both modulation and direct current (DC) amplitude, as well as phase. We decided to use the

logarithm of modulation amplitude and phase which are the typically considered values [25, 37, 42, 50, 51]. The forward solution produced by MCX consists actually of the path lengths traveled in each tissue type for each detected photon separately. From these, we can compute the amplitude with the Beer-Lambert law [37], and the phase (shift) is directly proportional to the mean path length of detected photons [50, 52]. MCX estimates the DC amplitude, but since our modulation frequency is small, we consider the amplitudes interchangeable [37].

The logarithm of amplitude $\ln(A)$ (or $\ln(\mathrm{SDD}^2 A)$) decreases, and the mean path length $<l>$ (amplitude-weighted mean $<l_A>$ as in [10] also considered) increases approximately linearly with respect to increasing source–detector distance (SDD) [25, 50]. The slopes of the fitted lines depend on the optical properties of the probed tissue [8, 25, 51]. The mathematical derivation of the linear relationships is based on several simplifying assumptions, such as modeling the tissue as a homogeneous infinite slab or semi-infinite medium [8] (several derivations for homogeneous infinite scattering and semi-infinite media have been presented; some references listed in [50]). However, since we and others have observed similar kind of linear behavior in practice [50], and others have successfully used the slopes for estimating homogeneous absorbing and scattering coefficients [25, 42, 51], we decided to use them in addition to the modulation amplitude and phase. Above all, the slopes provide single statistics describing the optical properties of the target, are simple to compare and do not depend on the absolute values of amplitude or phase.

In addition to the measurement values, we had to find suitable measures for the difference between a simulated value and the reference. The choice is especially relevant for comparison of vectors that have the amplitudes or phases for all source-detector pairs. Furthermore, we have to be able to determine the distance between optical parameter vectors in the sample space. Typical vector length measures, such as the Euclidean distance, are not ideal since the magnitudes of the terms in these vectors vary: Modulation amplitudes can differ by a factor of 10^5, and absorption and scattering coefficients generally differ by a factor of 100. Consequently, terms with largest magnitude would define the error term. Instead, we considered scale-independent relative difference measures. Yet, mean absolute relative difference is also problematic if the reference term is very small. To overcome this, we can take the tangent of the absolute relative difference. The error term, referred to as mean arctangent absolute percentage error (MAAPE) was introduced

in [53] and defined as

$$\text{MAAPE} = \frac{1}{N}\sum_{i=1}^{N} \arctan\left|\frac{p_{r,i} - p_{s,i}}{p_{r,i}}\right|, \tag{3.4}$$

where $p_{r,i}$ and $p_{s,i}$ refer to the reference and sampled value for the i^{th} parameter, respectively [53]. We have left out multiplication by 100 for convenience. Since the root mean squared error (RMSE) is a typical choice, we implemented it also for comparison with MAAPE. For parameter vectors, we only used MAAPE.

To conclude, we decided to test the following alternatives for the objective function:

- MAAPE and RMSE between sampled and reference logarithms of amplitudes for SDDs under 50 mm;
- MAAPE and RMSE between both mean and weighted mean path lengths for SDDs under 50 mm;
- RMSE between slopes fitted to (SDD, $\ln(A)$) and (SDD, $\ln(\text{SDD}^2 A)$) [25, 50] for SDD range 20–50 mm; and
- RMSE between slopes fitted to (SDD, $< l >$) and (SDD, $< l_A >$) for SDD range 20–50 mm.

The limited SDD range was used since the linearity appears after 20 mm, and we only use data under 50 mm to avoid problems with light leakage [50]. Slopes are calculated for each source separately, since this was observed to result in improved linear fits with respect to the R^2-value; typically the threshold of sufficient fit is set to 0.95 [25, 50] and using data from all sources practically never corresponded to such high values. Furthermore, this gives simpler optode arrangements; others have used only one or two sources with a few detectors in a row [25, 50]. Handling the sources separately could also be the approach for real data, since light coupling coefficients and calibration properties differ for each source and each detector [8, 50].

To evaluate the success of the random search, the intuitive question is that if we know the true values of the optical parameters, how close does the random search get. To evaluate closeness, we have to select an appropriate metric for distances between vectors. As was previously discussed, MAAPE is a potential alternative taking into account the variability in parameter magnitudes. In reality, we often do not know the exact true values, unless we are measuring a phantom. Yet, simulations enable studying the accuracy, at least with respect to the simulated measurables.

For this thesis, we developed the following method for evaluating accuracy: First sample $N+1$ parameter vectors, and pick one of them as the reference. Perform simulations and calculate the objective function value for each parameter set with respect to the reference. Find the best parameter vector—the one with the smallest error value. In addition, arrange the vectors in order with respect to increasing distance from the reference vector. Find the location, or index, of the best vector in the ordered list. To evaluate the accuracy of the result, we ask: In the sample space, to what percentage of the closest samples does the result belong to? Thus, we convert the index to an accuracy metric as

$$\text{accuracy} = 1 - \frac{i_{\text{best}}}{N}, \tag{3.5}$$

where i_{best} is the index of the result in the ordered list. The ratio is subtracted from 1 to get a range between 0 and 1 so that 1 corresponds to maximum accuracy. Of course, whether a high accuracy is actually good depends largely on the sample: On one hand, if the sampled ranges are too wide, the tested combinations might bee too arbitrary. On the other hand, if we have samples very close to the reference, many of the samples might estimate the true values within the accuracy of the metrics.

To summarize, if we had absolute data for all 17 subjects, the optical parameters would be estimated as follows:

1. Define range and select the mean and standard deviation for each coefficient.
2. Sample N values for each parameter from a Gaussian distribution.
3. Simulate the measurement values for each parameter combination.
4. Store the combination that gives values closest to the reference measurement.
5. Repeat for each subject separately.

The average of the parameters over the subjects should estimate the true values. The value of a certain parameter may vary between individuals [29], but if the values are very different, the whole approach has to be re-considered. Generally, the proposed algorithm is rather novel since repeated MC simulations have only become practical in the recent years due to the development of GPUs and massively parallel computation.

One tool for further studying the accuracy and sensitivity of the algorithm could be the the Jacobian matrices, or sensitivity profiles of the measurements to voxel-wise absorption or scattering coefficient changes [54, 55].

Jacobians are a good tool for inspecting measurement depth and sensitivity to changes in the tissue parameters. They are often used in difference imaging of brain activity. In the following, we introduce the algorithm for image reconstruction, which was also applied in the affective touch study.

3.4.2 Difference imaging

In this thesis, we only consider changes in the absorption coefficients in response to neuronal activation [10]. This is a typical choice since absorption shows most response to physiological changes and values can be directly converted to HbT perturbations, as discussed in sections 1 and 2.2.2. Other parameters, such as oxygen saturation, would require using at least two different wavelengths of input light.

The Jacobians $\mathbf{J}(s,d)$, for each source s and detector d, can be used to linearize the relationship between the voxel-wise absorption coefficient changes $\Delta\vec{\mu}_a$ and the measured changes in the logarithm of modulation amplitude $\Delta \log[A_{\mathrm{EXP}}(s,d)]$ [15, 29]. Each $\mathbf{J}(s,d)$ is a vector where each element corresponds to one voxel in the head model and gives the derivative of the measurable with respect to μ_a in the voxel. Consequently, the linearized inverse problem of reconstructing the absorption changes can in principle be solved via a matrix inversion. However, the inverse problem is extremely ill-posed, thus we utilize Tikhonov regularization and minimize the squared sum

$$\sum_{s,d}\left(\frac{\mathbf{J}(s,d)}{A_{\mathrm{MCX}}(s,d)}\Delta\vec{\mu}_a - \Delta\log\left[A_{\mathrm{EXP}}(s,d)\right]\right)^2 + \alpha\,||\mathbf{L}\Delta\vec{\mu}_a||_2^2\,. \tag{3.6}$$

The Jacobians and the simulated amplitudes $A_{\mathrm{MCX}}(s,d)$ are obtained with MCX. The matrix $\mathbf{L}$ is a discrete approximation of the Laplacian calculated as [10, 56]

$$L_{i,j} = \begin{cases} N_{\mathrm{n}}, & \text{if } i = j, \\ -1, & \text{if } j \text{ is a neighbor of } i, \\ 0, & \text{otherwise,} \end{cases}$$

where N_{n} is the number of neighboring voxels of voxel i in the 6-neighborhood. The parameter α, with value 10 in this thesis, is used to set an appropriate weight for the regularization term. We use MATLAB's lsqr-function [57] for minimizing equation 3.6.

In principle, the same approach could be applied in absolute imaging if the initial estimates for the parameters were sufficiently accurate. In practice, this is rarely the case, thus non-linear iterative methods as discussed in section 3.4.1 are employed.

Chapter 4

Implementation

The main programming platform in this thesis was MATLAB R2017b. All computation was outsourced to the Triton-cluster provided by the Aalto University School of Science "Science-IT" project [58]. This freed our local machine for other usage and enabled us to handle multiple subjects simultaneously as array jobs. Furthermore, Triton provided the multiple central processing units (CPU) required for the model deformations, and the graphics processing units (GPU) required for MCX. Yet, all computation (excluding photon simulations with MCX) could also be performed on ordinary workstations with a couple of CPUs. For the model deformations however, a modified lighter version of the algorithm would need to be used, as discussed in section 4.1.2. This chapter gives further details on the implementation of the grid search algorithm, and introduces the MCX software.

4.1 Model deformation with parameter grid search

We recall from section 3.2.1 that a grid search is performed to find the optimal affine parameters for registering the template to the target head surface. To start the search, we need an initial grid which is defined by the initial guesses and step lengths for each parameter, and the grid size. The most defining step is selecting the initial guesses: The grid size is mainly set by the available computation resources and time, and the appropriate step lengths depend on the size and the range as observed when estimating the initial guesses. Moreover, good initial guesses speed up the computation since we start closer to the optimum. They also enable us to guide the selection towards realistic values and avoid poor local minimums. Thus, we decided to perform a thorough search for the initial parameters, as described next.

4.1.1 Initial guesses for the affine transformation parameters

The essential starting point for the search is to understand the type of mismatch that each transformation addresses. To begin with, we recall from section 3.1 that we initially match the x-axes connecting the preauricular points, the y-axes connecting the nasion perpendicularly with the x-axis and the origins (O) according to the head system shown in Fig. 3.1A.

If the anatomical locations of the landmarks differ, this results in orientation and location errors between the template and the subject head, as demonstrated in Fig. 4.1. From the figure we observe that the mismatch can be fixed by first rotating the template (blue, subindex t) to the correct orientation, and then translating it to match the subject (pink, subindex s). Thus, rigid transformations fix absolute orientation errors which arise at the initial registration step, whereas anisotropic scaling accounts for the size and shape related differences. In the following, we explain the derivation of the initial estimates for all parameters using the head system definitions for the coordinate axes (Fig. 3.1A).

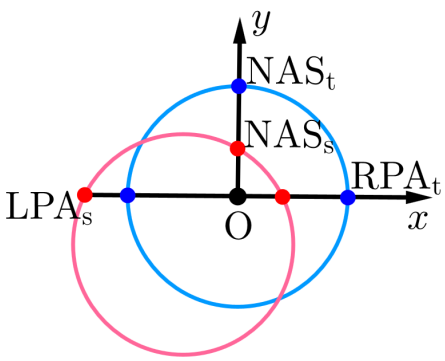

Figure 4.1 *See text on the left.*

At the beginning, all scaling parameters were set to 1. The idea was to fix the absolute orientation errors first, since it was easier to estimate the differences in the shape and size after the rigid transformations. We also wanted to avoid fixing absolute orientation errors with scaling; the head shapes should not differ remarkably in two-year-olds. The scaling parameters were then manually modified to find the best match according to visual evaluation.

The origins of the three main absolute orientation and location differences are visualized in Fig. 4.2: The arrows mark the misplacement or tilt that occurs when the selected landmark (red) differs from the real anatomical location (blue). In the first case in Fig. 4.2A, RPA has been selected more frontally than LPA, which rotates the target head with respect to the z-axis in the initial registration step. Intuitively, this can be fixed by rotating the template similarly with respect to the z-axis (accompanied by an appropriate translation). The aim is to make the line segment between the preauricular points in the template parallel to the corresponding true segment in the target. We calculated the first estimate for the angle r_z in radians as the

ratio of the relative difference between RPA and LPA along the head surface to the corresponding radius. The arc length was roughly estimated from the photographs, and the radius was calculated as the scaled distance between the template's preauricular points. The initial guess for the arc length was manually updated to reach a visually satisfying initial guess. The same approach was used for r_y when the relative difference was along the z-axis.

Rotations with respect to the x-axis fix the tilt due to inferior placement of preauricular points, as shown in the second case in Fig. 4.2B. When the tilted y-axis is matched with the template's y-axis, the target head is rotated by an angle r_x (using the nasion as the center of rotation). To fix this, the template has to be rotated similarly. To obtain the initial guess for r_x, we first calculated the average z-directional distance from the template's preauricular landmarks to the highest point on the template (largest z), and scaled this distance with s_z to obtain a "target value" for the corresponding length on the subject—with correct preauricular points. Then we measured the corresponding distance on the subject, and used the difference between this and the estimated "target" distance as the numerator in the ratio for the tangent of r_x. The denominator was calculated as the average y-directional distance from the subject's nasion to its preauricular points. The initial estimate for r_x was obtained as the inverse tangent of the ratio, and the value was updated by multiplication with a manually selected factor.

All in all, rotations fix errors caused by differences in the orientations of the matched head system axes. As has been mentioned, rotations have to be accompanied with an appropriate translation. We recall that a translation matching the template and target nasions was already added to our deformation procedure, as discussed in section 3.2.2. If the nasions have been selected accurately and the anatomies match, this should fix the remaining location error, which could be due to a too frontal placement of the preauricular points, as in Figs. 4.2B and 4.2C. The extra translations, which are

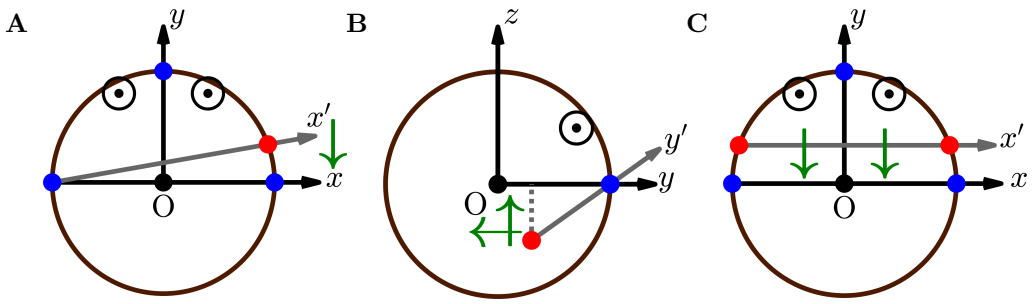

Figure 4.2 *The origin of errors that are fixed with rotation with respect to the z-axis* (A) *or x-axis* (B)*, or translation in y-direction* (C)*.*

left for optimization, are used to fix errors in the nasion sticker placement and anatomical nasion depth differences. The very first initial guesses for the translations were obtained from the photographs and again manually fixed to obtain a good match of the modified template with the target point set.

In chapter 5.1 we will observe that these initial parameters already decrease the SREs by a factor of four. Thus, they provide excellent starting points for the grid search. Clearly, we chose a rather laborious and hands-on approach for selecting the initial parameters, and the algorithm should also work with less-optimized initial guesses. However, this approach was beneficial for understanding and checking the deformations, and an efficient way to notice subject-specific special needs.

4.1.2 Parallel grid search and computational issues

To finalize the initial grid, the default grid parameters (see section 3.2.1) were selected as $g = 1$, $m = 3$, $d_s = 0.1$, $d_r = 0.2\,\text{rad}$ (11.5°), and $d_t = 10\,\text{mm}$. The maximum number of iterations was set to 20 and the lower threshold for improvement in cost to $\epsilon = 10^{-4}\,\text{mm}$. The maximum Delaunay sphere radius in the template surface mesh was set to 5 mm (2402 nodes, 4875 elements) for the optimization, though final results were computed with a maximum radius of 2 mm. This choice was observed to speed up the computation of the cost function, while the mesh still looked dense enough.

Despite the sparser mesh and having only three options for each parameter per grid, our implementation suffers from the curse of dimensionality: Since we have a large number of parameters (9), the grid size is $3^9 = 19683\,\text{points}$, which implies long computation times despite very fast cost function evaluations. To overcome the curse, we performed parallel computation with 18 CPUs required for each child. We handled four subjects simultaneously as array jobs, so the whole process had multiple levels of parallelization. Interestingly, similar challenges were not reported in [28, 33]. One reason for this could be the usage of distance maps which are only computed once [28]. Moreover, Mäkelä et al. only considered rigid registration with six parameters [28].

The required number of CPUs is high and such computational resources might not always be available. Yet, we discovered that the current slowness of the algorithm is due to re-computing the closest mesh points for each set of affine parameters. Thus, we wrote an **alternative cost function** which simply transforms the initially closest mesh points. We observed that this algorithm could be executed in roughly half of the time on one CPU (about 1.5 h) as the default on 18 parallel CPUs (about 4 h). Moreover, if the closest points were computed after a very good initial guess, the end results should

be roughly the same. However, if the initial mismatch of the template and the target is severe, the original closest points can not be used to guide the optimization—and the algorithm should not rely on an excellent initial guess. This thesis only presents results according to the default cost function.

4.1.3 Deforming a volume image in MATLAB

After the grid search, the final step was to deform the template—a 3D volume image—according to the found affine transformation parameters. We recall from section 3.1 that during the optimization, the mesh nodes are transformed in the template's coordinate system but with the origin set at the center of the head (see Fig. 3.1B). MATLAB provides functions for image warping, but they operate with respect to the template origin at the left upper corner of the $z = 0$ slice, when y-axis runs from left to right and x-axis downwards. Thus, we needed to modify the origin for the deformations, while also keeping the template origin at the original location, so that the frame is the same that the target points are given in. Specifically this means that the movement of the head caused by changes in the image canvas size had to be undone. We used a combination of affine3d- and imwarp-functions [59, 60] for scaling and rotation, and imtranslate-function [61] for translations.

Translations posed no problems, since they do not depend on the location of the origin. Scaling had to be followed by a translation to return the scaled head center to its original location. The most challenging were the rotations, since MATLAB modifies the image canvas size to fit the whole rotated image, and we loose information on the location of the head center with respect to the original template origin. Yet, assuming that the new canvas is the smallest that can fit the rotated original one, the original and new canvases are co-centric, thus we know the new location of the previous canvas center. If the new center is moved to this location, it corresponds to rotating the image with respect to its center. Moreover, if we move the image center to the head center prior to the rotations, the rotation is with respect to the head center, as wanted. Thus, we moved the image center to the head center, performed rotations with respect to the template origin, and translated the new center back to its original location. The image center was moved by modifying the original canvas size, and again movement of the head with respect to the template origin had to be canceled afterwards.

The used warping functions act in the left-handed image coordinate system, where the x-axis in the right-handed template coordinate system is the y-axis in the image, and vice versa. Thus, before each deformation, we permuted the x- and y-axis in the template. In addition, since the template has indices 0, 1, 3, 4 and 5, we suppressed the range for the deformations to 0–4

to avoid problems with interpolation, which is discussed next. In the end, we changed the axes and the range back to the original.

Deformation modifies the image grid, thus voxel values have to be estimated at new grid points with a combination of interpolation and resampling: Interpolation means fitting a continuous function to original grid points, and resampling refers to picking the new values according to the interpolated function. The function is often obtained with a convolution of the original values with an interpolation kernel. MATLAB's imwarp- and imtranslate-functions provide three alternatives for this kernel, corresponding to nearest neighbor, linear and cubic convolution interpolation, which was used in this thesis. The cubic interpolation kernel is a piece-wise third-degree polynomial, where four closest grid points are used to estimate the value at a new grid location [62, 63]. The process can be easily implemented as a matrix product and is efficient compared to general cubic spline interpolation [63].

Cubic convolution can model a second degree polynomial accurately, whereas linear and nearest neighbor interpolation only capture a first-degree or constant sampled function, respectively. It also has a better frequency performance, since the kernel's Fourier transformation is closer to the ideal low-pass filter [62–64]. However, we chose cubic convolution mainly based on visual comparison of deformed axial slices: Linear interpolation was observed to blur the image so that some detailed structures, such as CSF channels, vanished. These channels extend from the CSF layer to deeper parts of the brain, and since CSF has small scattering and absorption coefficients, they are relevant for the depth sensitivity of the measurements. Parker et al. observed similar kind of blurring and suggested using cubic convolution instead of linear [62]. On the other hand, we observed that nearest neighbor interpolation reconstructed the details relatively accurately, but the tissue boundaries where very rough, which again could have disturbed modeling the propagation of light in the head. Furthermore, we noticed an undesirable shift in the location of the head, as also reported in [62].

To summarize, cubic convolution was found to be the best compromise between conserving details and sufficient smoothness. The deformed head models can be directly used in MCX, which is introduced next along with details of our implementation.

4.2 Monte Carlo eXtreme

Monte Carlo eXtreme (MCX) is an open source software written in CUDA for GPU-accelerated photon propagation in massively parallel threads [3, 65, 66]. A GPU is a multi-core processor with total computing capability worth of

several CPUs [65]. We ran the MATLAB-version (MCXLAB) of the software on Nvidia Tesla P100 and V100 GPU-cards.

As has been mentioned in section 3.4, MCX implements the RTE, and the detailed rules of photon propagation are given in literature [39, 65, 67–69]. In short, instead of single photons, MCX propagates photon packets, which is a variance reduction technique called implicit capture [70]. The packet propagates in straight steps between scattering events, and a new scattering direction is calculated by picking the azimuth angle randomly between $[0, 2\pi)$ and the zenith angle from the Henyey-Greenstein phase function [39, 65, 67, 68]. At each voxel, a portion of the packet intensity is absorbed according to the Beer-Lambert law. If the intensity drops below a chosen limit, a Russian roulette [71] determines whether propagation is continued. Reflections are based on Fresnel's equations and enabled at the inner and outer tissue boundaries.

For each source, we simulate 10^9 photons [40, 72] for 90 ns using the collimated Gaussian beam source type. The source radius, or beam half-width, is set to 1.25 mm and the detector radius to 1.82 mm. The baseline optical parameters were given in Table 2.1. We use MCX to obtain the forward solutions—specifically the tissue-wise path lengths for each detected photon—which can be further utilized to compute the measurables or Jacobian matrices (see sections 3.4.1 and 3.4.2). The MCX settings are the same throughout this thesis, except for the tissue parameters.

To demonstrate the performace of DOT in imaging cortical activity (see section 3.4.2), we modeled an absorption increase of $8 \times 10^{-3}\,\mathrm{mm}^{-1}$ [10] in a spherical region on the superficial cortex of the atlas template. The sphere radius was set to 6 mm and restricted to gray matter voxels. We identified this region with its own index, and deformed the template to obtain individual perturbation models for each subject. We used MCX to estimate the detected amplitudes with and without the perturbation, and reconstructed the voxel-wise changes using the formula in Eq. 3.6. Photon shot noise was naturally included, and for amplitude this could be comparable to real measurement noise levels [10].

The voxel side length in the deformed models is 1 mm, and the Jacobians were calculated with this "resolution", but for the reconstructions the side length was increased to 2 mm to save memory and computation time [18, 40]. Jacobians were only computed with baseline parameters and assumed not to alter significantly due to the absorption perturbation [10]. The individual reconstructions were registered back to the reference atlas space for group-level statistical analysis. This is called spatial normalization [17].

Chapter 5

Results and Evaluation

5.1 Model deformation

Initially, most of the children had a good fit of the landmarks since the head coordinate systems (defined by the landmarks) were matched in the initial registration step. Otherwise the template was misplaced with respect to the surface points, which revealed the need for further registration. The initial surface registration errors (SREs) for the pearl marked points are given in Table 5.2.

To begin with, we consider the success of our initial guesses for the affine transformation parameters. Fig. 5.1 plots the resulting SREs for the pearl points for each individual, whereas Table 5.1 compares the initial and final mean SREs for all of the target points and for only the pearl points. Generally, the SREs decrease by a factor of four, thus we provide reasonable starting points for the grid search. The "fixed mesh"-column values are computed by modifying the original mesh instead of deforming and re-meshing the template as in the last two columns. We see that the results for the modified mesh and the modified template are similar, thus the approach of modifying the mesh during the optimization process is justified.

	Initial	Initial pearls	Fixed mesh	Fixed	Fixed pearls
SRE [mm]	7.5 ± 2.8	8.3 ± 3.6	2.3 ± 0.7	2.4 ± 0.7	2.5 ± 0.8

Table 5.1: *The average SREs over all 17 subjects, in the form mean $\pm$ std, originally and after the deformations according to the initial guesses.*

Next we consider the final results after the grid search. Fig. 5.1 plots the initial and final SREs for the pearl marked points with respect to the child index. Clearly, the errors drop dramatically, though most of the improvement

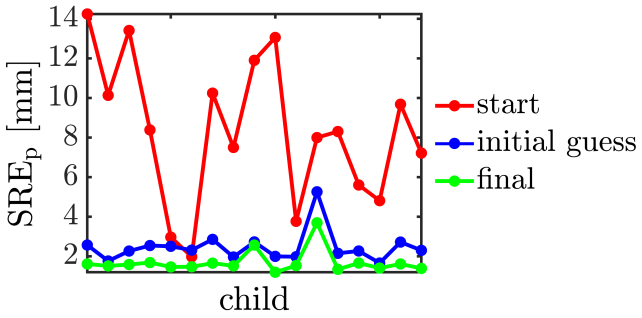

Figure 5.1 *The pearl SREs before and after model deformation.*

is achieved already with the initial guess. Yet, similar SREs do not necessarily correspond to the same set of affine parameters. Thus, the algorithm might find a more realistic combination even though the improvement in SRE is limited. Nevertheless, this plot does not fully reveal the usefulness of the heavy grid search algorithm.

Consequently, we repeated the computation with less-optimized general initial guesses. Specifically, we set all scale parameters to 1 and all translations and rotations to 0, except for $r_z = 0.2$ rad. The results are shown in Fig. 5.2. We see that the final SREs are very similar for both initial guesses, as clarified by the zoomed comparison in Fig. 5.2B; differences could be mainly due to computational inaccuracies in performing the deformation and meshing the template. Yet, the underlying affine transformation parameters are not the same, as shown by the medium absolute percentage errors (MdAPE, in decimals) of the parameters. Visual inspection reveals that the modified templates are very similar but might have emphasized different surface regions in the matching. With the optimized initial guess we can guide the result towards the most realistic solution. Yet, both of the presented result types should be sufficiently accurate for our needs. We also note that even the less-optimized initial guess is able to clearly improve some of the SREs: The rotation with respect to the z-axis and the nasion-match translation implemented in the initial deformation fix two of the most common absolute orientation errors caused by too frontal or inferior target preauricular points.

Fig. 5.3 visualizes the performance of the deformation for one subject with the optimized initial guess. The deformed mesh clearly matches the target point set (red points) better, and looks realistic in shape and size. This same subject was used to demonstrate the failure of the old cost function in chapter 3.2.2 and Fig. 3.3E, since the preauricular points were selected too frontally (too small y-coordinate in template coordinates) and inferior to (too large x-coordinate) their real locations. We fixed the resulting errors with

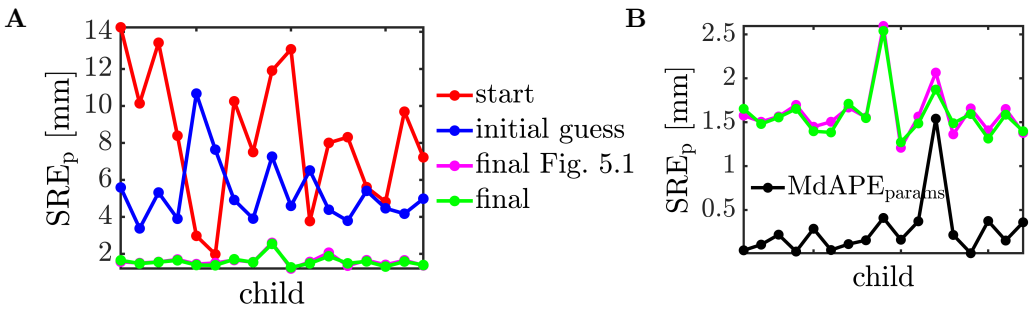

Figure 5.2 *Comparison of the pearl SREs for different initial guesses* (A). *The zoomed version* (B) *shows their similarity.*

rigid transformations, whereas the old algorithm scaled down the template in y-direction and stretched it in x-direction to match the landmarks and reach the highest pearl points simultaneously. This caused the elongated shape.

We performed similar visual evaluation for each subject, including comparison to original images. For one of the subjects, the 12th in order, the deformed head shape did not look completely realistic, mainly since she had

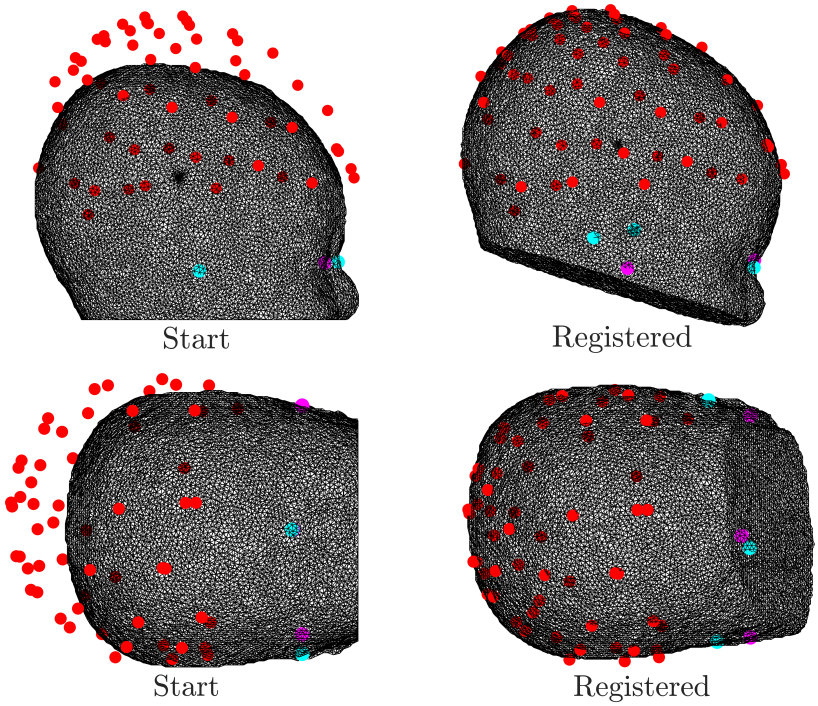

Figure 5.3 *Example of registering the template surface and landmarks (blue) to the pearls (red) and subject's landmarks (pink).*

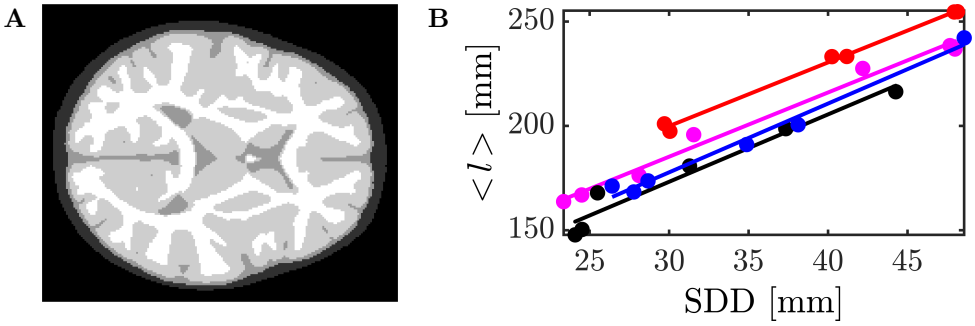

Figure 5.4 A. *An axial slice of the deformed template.* B. *Fitted lines for sources with R^2-values of 0.93 (red), 0.97 (pink), 0.98 (black) and 0.99 (blue).*

a braid on the right side of the head. To fix the shape, we modified the affine parameters manually; this result is shown in Fig. 5.1 and Table 5.2, whereas Fig. 5.2 compares the original results according to the algorithm. This specific subject also had a clearly wider head circumference compared to the distance between the preauricular points, which can be seen as a relatively large SRE for the preauricular points in Table 5.2; the points are inside the deformed template, since the template has to be wide enough to reach the pearl points.

The axial slices in the deformed models look sufficiently realistic and similar to the original template. However, narrow CSF voids towards deeper parts of the brain have occasionally diminished or vanished, as in Fig. 5.4A. This is due to limited accuracy of the image resampling, though cubic convolution was found to be relatively ideal. Aliasing occurs due to the rotations [73], which results in loss of detailed structure due to high spatial frequency suppression. Blocking appears as pixellation of the image and results from the fact that only a limited number of original image points (four in cubic) are used for the interpolation. In the end, visual inspection by human eye is not an objective measure of success since our eye is more tolerant of some type of noise and errors than other [62]. The real goal is to obtain physical similarity in the sense that propagation of light and anatomy are realistically modeled.

Table 5.2 collects statistics on the success of both the model deformation and the optode location estimation. The average distance from the pearl points to the meshed surface decreased from 8.3 ± 3.6 mm to 1.7 ± 0.6 mm, which is equal to the best accuracy reported in [32] and 0.2 mm greater than average shortest distance between mesh nodes of 1.5 ± 0.5 mm in [29]. Especially clear is the improvement in the standard deviation of the errors. Original hight values probably result from the orientation errors, since pearls might match the surface on one side and be clearly detached on the other.

Subject	Model deformation [mm]			Optode locations [mm]	
	$SRE_{p,init} \pm std$	$SRE_{p,final} \pm std$	$SRE_{PA,final}$	MAD_{grid}	$MED_{visible}$
1	14.2 ± 5.6	1.6 ± 1.7	2.0	0.8	3.2
2	10.1 ± 5.1	1.5 ± 1.2	0.9	1.0	4.3
3	13.4 ± 7.7	1.6 ± 1.1	1.7	0.3	8.1
4	8.4 ± 4.8	1.7 ± 1.5	1.2	0.4	4.2
5	3.0 ± 2.1	1.5 ± 1.1	0.6	1.1	7.1
6	2.0 ± 1.5	1.5 ± 1.2	0.6	0.8	4.7
7	10.2 ± 5.9	1.7 ± 1.2	1.6	0.3	4.5
8	7.5 ± 4.5	1.5 ± 1.2	0.7	0.5	2.0
9	11.9 ± 6.1	2.6 ± 2.5	1.6	0.5	4.0
10	13.1 ± 6.3	1.2 ± 1.0	0.4	0.5	3.6
11	3.8 ± 2.5	1.5 ± 1.3	0.4	0.7	2.2
12	8.0 ± 5.2	3.7 ± 3.1	6.5	0.7	5.0
13	8.3 ± 6.0	1.3 ± 1.0	0.5	0.4	5.1
14	5.6 ± 3.0	1.7 ± 1.4	1.8	0.6	3.6
15	4.8 ± 3.7	1.4 ± 1.1	2.1	0.6	12.5
16	9.7 ± 5.6	1.7 ± 1.3	0.4	0.3	4.3
17	7.2 ± 3.9	1.4 ± 1.1	1.0	0.7	3.1
MEAN	8.3 ± 3.6	1.7 ± 0.6	1.4	0.6	4.8

Table 5.2: *Statistics describing the success of the model registration and fiber interpolation. Columns in order: initial SRE for pearl marked surface points, final SRE for pearl points, final SRE for preauricular landmarks, mean absolute difference (MAD) between grid separations in flat probe versus on scaled head, and mean Euclidean distance (MED) from interpolated probe points to originally visible points.*

5.2 Optode localization

In Table 5.2, the mean absolute difference between optode separations on the grid versus on the scaled head surface, for the 25 nearest neighbors of each optode, is on average 0.6 mm, thus we can say that the known layout is reconstructed accurately enough, considering the inaccuracies related to modeling the bending of the probe. The mean Euclidean distances in the last column of Table 5.2 are between final points on the head surface and originally visible points on the outer surface of the probe, and would ideally

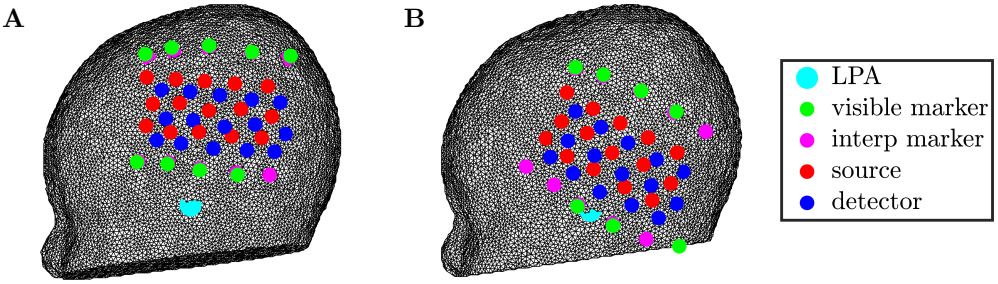

Figure 5.5 *Two examples of the interpolated optode locations.*

correspond to the probe thickness of 7 mm. The differences are probably due to inaccuracies in the photogrammetry and deformation according to the pearl points.

We further evaluated the success of the localization with visual comparison to photographs of the probe location for each subject. We compared the orientation of the probe and its location with respect to the left ear and additional facial markers. Generally, the results looked reasonable. Two examples of the optode layout are shown in Fig. 5.5A and Fig. 5.5B. The latter shows that the algorithm manages to fix the misplaced right-most marker on the bottom edge.

5.3 Estimation of optical parameters

Next, we consider the performance of the suggested random search algorithm for estimating the optical parameters. Instead of real measurements, the reference data was also simulated with MCX, sampling the reference from the same distribution that was used in the random search. Here we discuss the results for one of the subjects.

Table 5.3 collects the accuracies, according to equation 3.5, of the random search for the 10 different measurables listed in section 3.4.1: We consider MAAPE and RMSE (in brackets) for three absolute measurables, along with four slopes. In addition, for the slopes, we compare the accuracies obtained with all fitted lines versus only the ones exceeding the typical R^2-limit of $0.945 \approx 0.95$ for successful fit [25, 50]. The first three columns in Table 5.3 correspond to the average accuracy over all random samples, when one at a time is picked as the reference. The cases R1-R3 use different measures of closeness in the parameter vector space: R1 considers all tissue parameters, R2 excludes WM and R3 excludes WM and GM. For the last two columns, we randomly picked one of the samples, and repeated the simulation for the corresponding parameter set to test the algorithms tolerance to statistical

noise. E1 and E2 refer to two different exact references; all tissue parameters were included to the closeness measure.

Objective function	**Accuracy** (Cases R1-R3, E1-E2)				
	R1	R2	R3	E1	E2
Absolute values MAAPE (RMSE)					
$\ln(A)$	0.81 (0.81)	0.97 (0.97)	0.82 (0.82)	1 (1)	1 (1)
$<l_A>$	0.81 (0.77)	0.92 (0.86)	0.83 (0.76)	1 (0.72)	1 (0.95)
$<l>$	0.88 (0.89)	0.93 (0.93)	0.79 (0.77)	1 (1)	1 (1)
Slope (SDD, y) RMSE ($\mathrm{R}^2_{\mathrm{th}} = 0.945$)					
$y = \ln(A)$	0.73 (0.68)	0.84 (0.79)	0.71 (0.67)	0.93 (0.96)	0.51 (0.20)
$y = \ln(\mathrm{SDD}^2 A)$	0.73 (0.59)	0.84 (0.64)	0.71 (0.49)	0.93 (0.89)	0.51 (0.29)
$y =< l_A >$	0.67 (0.53)	0.72 (0.53)	0.61 (0.44)	0.75 (0.40)	0.41 (0.14)
$y =< l >$	0.84 (0.64)	0.87 (0.65)	0.64 (0.52)	1 (0.20)	1 (0.97)

Table 5.3: *Accuracy of the random search for optical parameters. Cases R1-R3 show average accuracy over 801 different references; in cases E1–E2, the exact replicate of the reference was included in the sample.*

The results in the columns R1, R2 and R3 suggest that the measurables are not very sensitive to WM in the two-year-old model. However, they depend on GM, thus the sensitivity is not limited to the surface. Yet, the standard deviations of the WM sampling distributions were significantly greater than for the two other tissue types. Next, we should repeat the study for constant standard deviations, of for example 10%.

The slopes perform poorer than absolute values, which can result from various reasons: Previously, the slopes have been used to estimate the parameter values—not to distinguish sets from another. Furthermore, the fitted slopes present the optical properties of the probed head volume as a whole (homogeneous), but there is no guarantee that the optical parameter set corresponding to the slope would be unique. However, slope estimation gets more accurate when we remove the R^2-threshold for line fit success, thus increase the number of slopes used in the comparison. Thus, though a high threshold is justified when the parameter values are calculated straight from the slopes, in our approach of indirect estimation, we suggest using a lower threshold for better performance.

Based on this table, we suggest using absolute values of modulation amplitude and phase along with the slope fitted to mean path length data.

Examples of the latter fit are given in Fig. 5.4B. Yet, the standard deviations in the sampled space are rather small, thus a low accuracy here could be sufficient in practice. Further study should investigate the sensitivity and resolution of this method further.

5.4 Example of reconstructed simulated activation

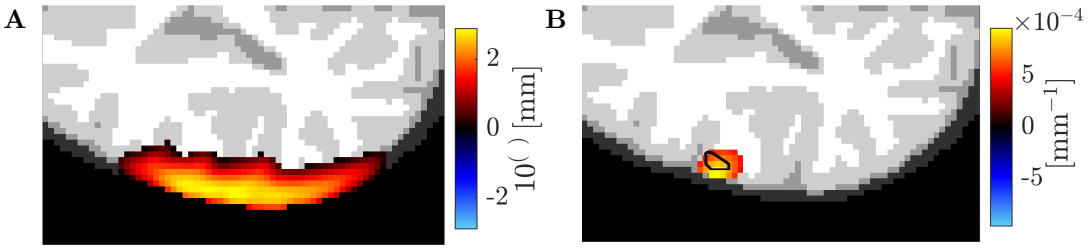

Figure 5.6 *The Jacobians* (A) *were used to reconstruct the simulated high-contrast absorption perturbation marked with a black line* (B).

Figure 5.6A visualizes the spatially normalized, average 10-based logarithm of the Jacobian over the 17 subjects. Logarithm was used to improve the information content of the image. The visualization threshold was set to 1% of the maximum value. Figure 5.6B shows the spatially normalized, mean reconstructed voxel-wise μ_a changes on the atlas template. The visualization threshold was set at one half of the maximum absolute reconstructed value, similarly as in [18]. The reconstruction seems fairly successful: The reconstructed region is restricted close to the simulated perturbation, with the maximum value located 2 mm away from the nearest simulated voxel. However, contrast is reduced by a factor of 8, or approximately 4 for the individual results with the deformed models.

Spatial normalization most likely affects the resolution of the reconstruction: First, the Jacobian is computed on the deformed model with a resolution of 1 mm. Then, the voxel side length is increased to 2 mm, and the reconstruction is computed. After this, the result is deformed back to the template, which includes changing the resolution to 1 mm and back to 2 mm after the deformation, since the inverse deformation has to be performed in the original resolution. The amount of inaccuracy introduced by these multiple transformations should be further studied. However, the success of the reconstruction in the simulated case is promising.

Chapter 6

Discussion

This thesis presented three algorithms for generating the optical head model for DOT: registration of an atlas template to the subject's head surface, interpolation of the optode locations and estimation of the optical parameters. The first two were applied to 17 two-year-olds participating in the FinnBrain affective touch study. Compared to results with previous simpler models, the enhanced models modified the regions reconstructed to respond to affective touch and restricted the activity better to gray matter, which shows that DOT is very sensitive to the accuracy of the optical model. In this chapter, we will further discuss the chosen approaches and remaining challenges.

The accuracy of photogrammetry is essential for the success of presented methods, since it was used to reconstruct the target points for surface registration and the probe markers for optode interpolation. Accuracies as good as 0.25 ± 0.05 mm have been reported [7], whereas we have initial results suggesting an accuracy of 1.3 mm with respect to CT. Our in-house three-camera system reached 1–2 mm, but generally three cameras should perform more accurately. We have also planned to build a 11-camera system where one simultaneous photo shot with all the cameras would be enough to reconstruct the head surface. The problem with the current stereoscopic imaging is that we have to take multiple photographs with a hand-held system, and it is challenging to keep the child stable during the process.

The pearl mesh cap used in the study has many advantages: It is comfortable for the subject, while enabling relatively tight contact to the head surface since the hair is guided trough the holes. However, for many subjects, we had rather few points from the back of the head, mainly because some pearls had dropped off or hair covered them. In the former case, we could have tried using the visible empty mesh knots. An even distribution of target points is important so that different regions have an equal weight in the registration—unless we want to emphasize the probed region.

There are further problems related to the pearls: It can be difficult to select exactly the same spots of the pearl when performing photogrammetry. The reconstructed location has to be dropped radially to the surface, and our sphere-fitting approach (see section 3.1) also has various sources of inaccuracy. In addition, hair can lift the pearls, or move individual pearls or the whole mesh during the photo shoot. Furthermore, one subject had the mesh inside-out, but this was measured not to affect the needed length in radial drop of pearl points. At least regions without hair could possibly be marked with circular reflective marker stickers instead of pearls [7].

After photogrammetry, we used a non-rigid affine transformation to register the template to the target points. This approach has limited ability to modify the shape of the head, thus the next approach could be to use more advanced elastic free-form deformations representing the template surface with linear or non-linear B-spline basis functions [18, 33]. Yet, here the accuracy of the target set is increasingly important. Nevertheless, elasticity would be beneficial for neonatal models since their head shapes differ more, especially depending on the method of birth. It could also enable modeling the anatomical differences in the nasion depth which prevented us from minimizing exact nasion separation. If the landmarks have been chosen accurately, their point-wise registration would most likely be beneficial [33].

For the targets in this thesis, the inaccuracy in the preauricular points was often rather severe, which resulted in clear location and orientation errors at the initial registration step. Consequently, the rigid transformations (rotation and translation) were most important in the registration. If the initial guess for the affine parameters is poor, the grid search might end in a local minimum where absolute orientation errors are fixed with scaling. A possible solution would be to optimize the rigid parameters first, and use the result to guide further optimization. Alternatively, we could attempt to fix the misplaced landmarks already before the initial registration step.

With the default iterative computation of the closest mesh points, the presented grid search suffers from the curse of dimensionality. Yet, we introduced an alternative cost function that overcame the curse by simply minimizing the distance to the originally closest mesh points—without mesh transformation (see section 4.1.2). If the initial guess for the parameters is very good, we suggest considering whether the computationally heavier algorithm is necessary. A compromise would be to update the closest points less frequently. An option for more efficient sampling would be to randomly select the parameters from uniform distributions instead of the grid search [49]. However, we consider the current combination of partly manually selected initial guesses and a grid search practical enough and, above all, successful in performance.

To get more accurate estimates for the success of the model registration, we would need to have the anatomical images for each subject. The geometrical accuracy could be estimated from the distances between closest mesh nodes on the deformed and real meshes [29]. Furthermore, their accuracy in modeling light propagation could be estimated as the similarity of the measurement sensitivity profiles [29]. Finally, the ultimate measure of success is the similarity of reconstructed images. The correlation of the accuracies is also of interest [29]; does an accurate match of the geometries (as we have small SREs) guarantee successful image reconstruction? We could also further study how well the internal structures are reproduced.

Finally, the whole idea of atlas-based modeling contains some issues for consideration: We can not be sure that the interior of the brain deforms in a predictable way based on the exterior surface. Some individual anatomical features are missing from the deformed template. Furthermore, image resampling causes blurring, aliasing and other losses in anatomical details when we deform the template (see section 4.1.3). Similar losses are introduced when the reconstructed result is deformed back to the common template. Consequently, it is relevant to consider alternative approaches for avoiding resampling: MCX has been reported to enable anisotropic voxel side length scales in the future. Then, instead of scaling the template, we could just give MCX the scaling parameters. Alternatively, we could generate a volumetric tetrahedral mesh of the template, and use the transformed nodes to define the volume mesh for the registered model. Yet, we would still have to resample the voxel model from the modified mesh.

To finish the discussion on the model registration, we comment that the algorithm could be used for other purposes as well. For example, segmentation of an individual's anatomical image can be guided by first deforming a segmented template to match the surface of the subject's head. Shi et al. used the two-year-old template to segment the one-year-old and neonatal images, which typically have poorer quality than the two-year-olds' [17].

The interpolated locations of the optodes on the registered template surface are highly dependent on the visible markers that have been reconstructed with photogrammetry. Yet, the probe might be detached from the head, especially at the top, thus all markers might not be on the head surface. Furthermore, if the landmark positions move between the pearl mesh and the probe images, this disturbs the co-registration of the probe points on to the head. This effect is currently under study. The accuracy of the fiber interpolation was difficult to evaluate since we did not know the real locations of the optodes. Yet, we took CT images of a doll head (see Fig. 3.5C) with the probe, and plan to evaluate the accuracy by comparing the interpolated locations to the ones extracted from the CT images.

In the interpolation algorithm, the fitted sphere has a significant role, especially since all the projections are performed radially towards its center. A possibly more accurate approach would be to use the normal directions of the triangular mesh elements instead—the sphere could be used just for the spherical coordinates in the optimization phase. Yet, especially for the initial guess, when the fitted plane is projected to the head surface, a radial drop—or projecting the points to the fitted sphere first—could be beneficial in guiding the optodes to maintain the probe layout. During the optimization, the projection direction should not make a big difference, since the drop distances are short and the sphere fits the probed region of the surface well.

The same consideration applies for the source input directions: Theoretically, a more justified approach would be to use the facial normal of the triangular element within which each source lies. Yet, in a dense mesh, the normal directions might not point inside the head in the intuitive manner since the deformed voxelated surface is rough. On the other hand, the probe might not match the surface of the head exactly. Generally, the radial directions offer a safe and presumably rather accurate alternative, but this should anyways be further studied.

As the final part this thesis, we prepared an algorithm for estimating the optical parameters via random search. The presented work left open a lot of questions on, for example, the sensitivity of the algorithm to different tissue types and the resolution of the method. The random search could be developed further, for example, by iterating it with updated distributions, similarly as in the model deformation, where the grid gets denser with each iteration. Alternatively, a grid search approach could be applicable with fewer photons. To improve the signal-to-noise ratio, we could obtain the simulated and real data as the average or median of, for example, 10 forward solutions [25]. Finally, instead of considering differences between measured and fitted values, we could develop more advanced objective functions, which could, for example, implement prior knowledge of noise behaviour via Bayesian statistics. We should also consider the sufficiency of the search range and the number of simulated photons.

Real measurements will introduce further challenges to the estimation. These include modeling different noise types, instrumental factors such as coupling errors and light leakage, and the effect of hair (color) on the optical parameters [50]. Some variability is expected to occur between subjects within an age group, and for the same tissue type at different locations.

To conclude, clearly there is always some inaccuracy in the obtained anatomical model, optode locations and optical parameters. Approximation error methods could be utilized to handle the remaining inaccuracies in the optical model [74, 75].

Chapter 7

Conclusions

Diffuse optical tomography (DOT) provides a practical functional brain imaging modality for young children. Neuronal activity perturbs the local hemodynamic parameters, which affects the optical properties. In DOT, tissue is illuminated with near-infrared light, and changes in the amplitude and phase of detected light are reconstructed into volumetric maps of perturbations in the optical parameters. Successful image reconstruction requires an accurate optical model, which consists of the distribution of optical properties and the locations of the light sources and detectors. This thesis presented practical methods for generating the model. The target group consisted of 17 two-year-olds, but the methods are applicable to other age groups as well.

The segmented anatomical models were obtained by registering an age-appropriate atlas template to points measured with photogrammetry from the subject's head. A grid search was implemented to minimize the weighted sum of the average distance from a target point to the template (SRE), and the separation between template and target nasions. Optodes were localized by minimizing the differences between optode separations along the surface versus on the flat probe, and the distance to extra markers reconstructed with photogrammetry. Finally, we prepared an algorithm for randomly sampling parameter sets from Gaussian distributions, and estimating the baseline optical parameters by fitting simulated values to reference data.

The registration decreased the SRE from $8.3 \pm 3.6\,\mathrm{mm}$ to $1.7 \pm 0.6\,\mathrm{mm}$, on average over all subjects. Interpolated optode locations corresponded to the known layout with an average error of 0.6 mm. The random search algorithm showed potential in estimating at least the joint scalp and skull, and gray matter parameters. Further work should study the sensitivity of the method and combine it with real measurement data. Reliable optical parameter estimation would be important for scientific and clinical applications of DOT.

Bibliography

[1] iso2mesh toolbox. `http://iso2mesh.sourceforge.net/cgi-bin/index.cgi`. Accessed: 2018-05-01.

[2] metch toolbox. `http://iso2mesh.sourceforge.net/cgi-bin/index.cgi?metch`. Accessed: 2018-04-20.

[3] Monte Carlo eXtreme (MCX) software. `http://mcx.sourceforge.net/cgi-bin/index.cgi`. Accessed: 2017-02-09.

[4] S. Lloyd-Fox, A. Blasi, and C. E. Elwell. Illuminating the developing brain: The past, present and future of functional near infrared spectroscopy. *Neuroscience and Biobehavioral Reviews*, 34(3):269–284, 2010.

[5] S. Lloyd-Fox, J. E. Richards, A. Blasi, D. G. M. Murphy, C. E. Elwell, and M. H. Johnson. Coregistering functional near-infrared spectroscopy with underlying cortical areas in infants. *Neurophotonics*, 1(2):025006, 2014.

[6] E. H. Jönsson, K. Kotilahti, J. Heiskala, H. Backlund Wasling, H. Olausson, I. Croy, H. Mustaniemi, P. Hiltunen, J. J. Tuulari, N. M. Scheinin, L. Karlsson, H. Karlsson, and I. Nissilä. Affective and non-affective touch evoke differential brain responses in 2-month-old infants. *NeuroImage*, 169:162–171, 2018.

[7] A. Y. Bluestone, G. Abdoulaev, C. H. Shmitz, R. L. Barbour, and A. H. Hielscher. Three-dimensional optical tomography of hemodynamics in the human head. *Optics Express*, 9(6):272–286, 2001.

[8] T. Durduran, R. Choe, W. B. Baker, and A. G. Yodh. Diffuse optics for tissue monitoring and tomography. *Reports on Progress in Physics*, 73(7):076701, 2010.

[9] I. Nissilä, T. Noponen, J. Heino, T. Kajava, and T. Katila. Diffuse optical imaging. In J. C. Lin, editor, *Advances in Electromagnetic Fields in Living Systems*, volume 4, pages 77–129. Springer, 2005.

[10] J. Heiskala, P. Hiltunen, and I. Nissilä. Significance of background optical properties, time-resolved information and optode arrangement in diffuse optical imaging of term neonates. *Physics in Medicine and Biology*, 54(3):535–554, 2009.

[11] F. F. Jöbsis. Noninvasive, infrared monitoring of cerebral and myocardial oxygen sufficiency and circulatory parameters. *Science*, 198(4323):1264–1267, 1977.

[12] J. C. Hebden, A. Gibson, R. M. Yusof, N. Everdell, E. M. C. Hillman, D. T. Delpy, S. R. Arridge, T. Austin, J. H. Meek, and J. S. Wyatt. Three-dimensional optical tomography of the premature infant brain. *Physics in Medicine and Biology*, 47(23):4155–4166, 2002.

[13] H. Singh, R. J. Cooper, C. W. Lee, L. Dempsey, A. Edwards, S. Brigadoi, D. Airantzis, N. Everdell, A. Michell, D. Holder, J. C. Hebden, and T. Austin. Mapping cortical haemodynamics during neonatal seizures using diffuse optical tomography: A case study. *NeuroImage: Clinical*, 5:256–265, 2014.

[14] M. Stenroos and J. Sarvas. Bioelectromagnetic forward problem: isolated source approach revis(it)ed. *Physics in Medicine and Biology*, 57(11):3517–3535, 2012.

[15] A. P. Gibson, J. C. Hebden, and S. R. Arridge. Recent advances in diffuse optical imaging. *Physics in Medicine and Biology*, 50(4):1–43, 2005.

[16] J. Heiskala, M. Pollari, M. Metsäranta, P. E. Grant, and I. Nissilä. Probabilistic atlas can improve reconstruction from optical imaging of the neonatal brain. *Optics Express*, 17(17):14977–14992, 2009.

[17] F. Shi, P.-T. Yap, G. Wu, H. Jia, J. H. Gilmore, W. Lin, and D. Shen. Infant Brain Atlases from Neonates to 1- and 2-Year-Olds. *PLoS ONE*, 6(4):e18746, 2011.

[18] S. L. Ferradal, A. T. Eggebrecht, M. Hassanpour, A. Z. Snyder, and J. P. Culver. Atlas-based head modeling and spatial normalization for high-density diffuse optical tomography: *In vivo* validation against fMRI. *NeuroImage*, 85:117–126, 2014.

[19] L. Karlsson, M. Tolvanen, N. M. Scheinin, H.-M. Uusitupa, R. Korja, E. Ekholm, J. J. Tuulari, M. Pajulo, M. Huotilainen, T. Paunio, and H. Karlsson. Cohort Profile: The FinnBrain Birth Cohort Study (FinnBrain). *International Journal of Epidemiology*, 47(1):15–16j, 2017.

[20] L. Pirazzoli, S. Lloyd-Fox, R. Braukmann, M. H. Johnson, and T. Gliga. Hand or spoon? Exploring the neural basis of affective touch in 5-month-old infants. *Developmental Cognitive Neuroscience*, 2018, in press.

[21] K. MacLean. The impact of institutionalization on child development. *Development and Psychopathology*, 15(4):853–884, 2003.

[22] I. Nissilä, K. Kotilahti, K. Fallström, and T. Katila. Instrumentation for the accurate measurement of phase and amplitude in optical tomography. *Review of Scientific Instruments*, 73(9):3306–3312, 2002.

[23] I. Nissilä, T. Noponen, K. Kotilahti, T. Katila, L. Lipiäinen, T. Tarvainen, M. Schweiger, and S. Arridge. Instrumentation and calibration methods for the multichannel measurement of phase and amplitude in optical tomography. *Review of Scientific Instruments*, 76(4):044302, 2005.

[24] E. M. C. Hillman, A. Devor, M. B. Bouchard, A. K. Dunn, G. W. Krauss, J. Skoch, B. J. Bacskai, A. M. Dale, and D. A. Boas. Depth-resolved optical imaging and microscopy of vascular compartment dynamics during somatosensory stimulation. *NeuroImage*, 35(1):89–104, 2007.

[25] P. Farzam, E. M. Buckley, P.-Y. Lin, K. Hagan, P. E. Grant, T. E. Inder, S. A. Carp, and M. A. Franceschini. Shedding light on the neonatal brain: probing cerebral hemodynamics by diffuse optical spectroscopic methods. *Scientific Reports*, 7:15786, 2017.

[26] J. Steinbrink, H. Wabnitz, H. Obrig, A. Villringer, and H. Rinneberg. Determining changes in NIR absorption using a layered model of the human head. *Physics in Medicine and Biology*, 46(3):879–896, 2001.

[27] A. P. Gibson, J. Riley, M. Schweiger, J. C. Hebden, S. R. Arridge, and D. T. Delpy. A method for generating patient-specific finite element meshes for head modelling. *Physics in Medicine and Biology*, 48(4):481–495, 2003.

[28] T. Mäkelä, P. Clarysse, J. Lötjönen, O. Sipilä, K. Lauerma, H. Hänninen, E.-P. Pyökkimies, J. Nenonen, J. Knuuti, T. Katila, and I. E. Magnin. A New Method for the Registration of Cardiac PET and MR

Images Using Deformable Model Based Segmentation of the Main Thorax Structures. In W. Niessen and M. Viergever, editors, *International Conference on Medical Image Computing and Computer-Assisted Intervention*, pages 557–564. Springer, 2001.

[29] X. Wu, A. T. Eggebrecht, S. L. Ferradal, J. P. Culver, and H. Dehghani. Evaluation of rigid registration methods for whole head imaging in diffuse optical tomography. *Neurophotonics*, 2(3):035002, 2015.

[30] Medical Dictionary (TheFreeDictionary by Farlex). `https://medical-dictionary.thefreedictionary.com`. Accessed: 2018-11-28.

[31] X. Wu, A. T. Eggebrecht, S. L. Ferradal, J. P. Culver, and H. Dehghani. Quantitative evaluation of atlas-based high-density diffuse optical tomography for imaging of the human visual cortex. *Biomedical Optics Express*, 5(11):3882–3900, 2014.

[32] X. Wu, A. T. Eggebrecht, S. L. Ferradal, J. P. Culver, and H. Dehghani. Atlas-based high-density diffuse optical tomography for imaging the whole human cortex. In B. J. Tromberg, A. G. Yodh, E. M. Sevick-Muraca, and R. R. Alfano, editors, *Optical Tomography and Spectroscopy of Tissue XI*, volume 9319, pages 1–6. International Society for Optics and Photonics, 2015.

[33] J. Koikkalainen and J. Lötjönen. Reconstruction of 3-D Head Geometry From Digitized Point Sets: An Evaluation Study. *IEEE Transactions on Information Technology in Biomedicine*, 8(3):377–386, 2004.

[34] Q. Fang. Mesh-based Monte Carlo method using fast ray-tracing in Plücker coordinates. *Biomedical Optics Express*, 1(1):165–175, 2010.

[35] A. N. Yaroslavsky, P. C. Schulze, I. V. Yaroslavsky, R. Schober, F. Ulrich, and H. J. Schwarzmaier. Optical properties of selected native and coagulated human brain tissues in vitro in the visible and near infrared spectral range. *Physics in Medicine and Biology*, 47(12):2059–2073, 2002.

[36] J. Heiskala, K. Kotilahti, and I. Nissilä. An application of perturbation Monte Carlo in optical tomography. In *Proc. IEEE Engineering in Medicine and Biology 27th Annual Conference*, volume 27, pages 274–277. IEEE, 2005.

[37] J. Heiskala, K. Kotilahti, L. Lipiäinen, P. Hiltunen, P. E. Grant, and I. Nissilä. Optical tomographic imaging of activation of the infant auditory cortex using perturbation Monte Carlo with anatomical a priori information. In B. W. Pogue and R. Cubeddu, editors, *Diffuse Optical Imaging in Tissue*, volume 6629. International Society for Optics and Photonics, 2007.

[38] Y. Fukui, Y. Ajichi, and E. Okada. Monte Carlo prediction of near-infrared light propagation in realistic adult and neonatal head models. *Applied Optics*, 42(16):2881–2887, 2003.

[39] J. Heiskala. *Accurate modelling of tissue properties in diffuse optical imaging of the human brain.* PhD thesis, Helsinki University of Technology, Department of Biomedical Engineering and Computational Science, 2009.

[40] A. Custo, W. M. Wells III, A. H. Barnett, E. M. C. Hillman, and D. A. Boas. Effective scattering coefficient of the cerebral spinal fluid in adult head models for diffuse optical imaging. *Applied Optics*, 45(19):4747–4755, 2006.

[41] F. E. W. Schmidt. *Development of a Time-Resolved Optical Tomography System for Neonatal Brain Imaging.* PhD thesis, University of London, Department of Medical Physics and Bioengineering, 1999.

[42] M. A. Franceschini, S. Thaker, G. Themelis, K. K. Krishnamoorthy, H. Bortfeld, S. G. Diamond, D. A. Boas, K. Arvin, and P. E. Grant. Assessment of Infant Brain Development With Frequency-Domain Near-Infrared Spectroscopy. *Pediatric Research*, 61(5):546–551, 2007.

[43] F. Tadel, S. Baillet, J. Mosher, D. Pantazis, and R. M. Leahy. Brainstorm: A user-friendly application for MEG/EEG analysis. *Computational Intelligence and Neuroscience*, 2011:1–13, 2011.

[44] Q. Fang and D. A. Boas. Tetrahedral mesh generation from volumetric binary and grayscale images. In *Proceedings of IEEE International Symposium on Biomedical Imaging 2009: From Nano to Macro*, pages 1142–1145. IEEE, 2009.

[45] point2trimesh-function by Daniel Frisch. `https://se.mathworks.com/matlabcentral/fileexchange/52882-point2trimesh-distance-between-point-and-triangulated-surface`. Accessed: 2018-04-20.

[46] The sketch of the preauricular point. `http://www.fieldtriptoolbox.org/faq/how_are_the_lpa_and_rpa_points_defined`. Accessed: 2018-11-21.

[47] absor-function by Matt J. `https://se.mathworks.com/matlabcentral/fileexchange/26186-absolute-orientation-horn-s-method`. Accessed: 2015-06-16.

[48] fminsearch-function. `https://se.mathworks.com/help/matlab/ref/fminsearch.html`. Accessed: 2018-11-25.

[49] J. Bergstra and Y. Bengio. Random search for hyper-parameter optimization. *Journal of Machine Learning Research*, 13(Feb):281–305, 2012.

[50] T. Noponen, K. Kotilahti, I. Nissilä, T. Kajava, and P. Meriläinen. Effects of improper source coupling in frequency-domain near-infrared spectroscopy. *Physics in Medicine and Biology*, 55(10):2941, 2010.

[51] S. Fantini, M.-A. Franceschini, J. S. Maier, S. A. Walker, B. B. Barbieri, and E. Gratton. Frequency-domain multichannel optical detector for noninvasive tissue spectroscopy and oximetry. *Optical Engineering*, 34(1):32–42, 1995.

[52] S. R. Arridge, M. Cope, and D. T. Delpy. The theoretical basis for the determination of optical pathlengths in tissue: temporal and frequency analysis. *Physics in Medicine and Biology*, 37(7):1531–1560, 1992.

[53] S. Kim and H. Kim. A new metric of absolute percentage error for intermittent demand forecasts. *International Journal of Forecasting*, 32(3):669–679, 2016.

[54] R. Yao, X. Intes, and Q. Fang. Direct approach to compute Jacobians for diffuse optical tomography using perturbation Monte Carlo-based photon "replay". *Biomedical Optics Express*, 9(10):4588–4603, 2018.

[55] R. Yao, X. Intes, and Q. Fang. A Rapid Approach to Build Jacobians for Optical Tomography via Monte Carlo Method and Photon "Replay". In *Bio-Optics: Design and Application*, pages BoW3A–3. Optical Society of America, 2017.

[56] T. Näsi, H. Mäki, P. Hiltunen, J. Heiskala, I. Nissilä, K. Kotilahti, and R. J. Ilmoniemi. Effect of task-related extracerebral circulation on diffuse optical tomography: experimental data and simulations on the forehead. *Biomedical Optics Express*, 4(3):412–426, 2013.

[57] lsqr-method. `https://se.mathworks.com/help/matlab/ref/lsqr.html`. Accessed: 2018-12-05.

[58] Aalto Science-IT project and Triton cluster. `http://science-it.aalto.fi`. Accessed: 2018-11-29.

[59] affine3d-function. `https://se.mathworks.com/help/images/ref/affine3d.html`. Accessed: 2018-11-26.

[60] imwarp-function. `https://se.mathworks.com/help/images/ref/imwarp.html`. Accessed: 2018-11-25.

[61] imtranslate-function. `https://se.mathworks.com/help/images/ref/imtranslate.html`. Accessed: 2018-11-25.

[62] J. A. Parker, R. V. Kenyon, and D. E. Troxel. Comparison of interpolating methods for image resampling. *IEEE Transactions on Medical Imaging*, 2(1):31–39, 1983.

[63] R. G. Keys. Cubic convolution interpolation for digital image processing. *IEEE Transactions on Acoustics, Speech, and Signal Processing*, ASSP-29(6), 1981.

[64] E. Meijering and M. Unser. A note on cubic convolution interpolation. *IEEE Transactions on Image processing*, 12(4):477–479, 2003.

[65] Q. Fang and D. A. Boas. Monte Carlo simulation of photon migration in 3D turbid media accelerated by graphics processing units. *Optics Express*, 17(22):20178–20190, 2009.

[66] L. Yu, F. Nina-Paravecino, D. Kaeli, and Q. Fang. Scalable and massively parallel Monte Carlo photon transport simulations for heterogeneous computing platforms. *Journal of Biomedical Optics*, 23(1):010504, 2018.

[67] L. Wang, S. L. Jacques, and L. Zheng. MCML-Monte Carlo modeling of light transport in multi-layered tissues. *Computer Methods and Programs in Biomedicine*, 47(2):131–146, 1995.

[68] D. A. Boas, J. P. Culver, J. J. Stott, and A. K. Dunn. Three dimensional Monte Carlo code for photon migration through complex heterogeneous media including the adult human head. *Optics Express*, 10(3):159–170, 2002.

[69] M. Hiraoka, M. Firbank, M. Essenpreis, M. Cope, S. R. Arridge, P. Van Der Zee, and D. T. Delpy. A Monte Carlo investigation of optical pathlength in inhomogeneous tissue and its application to near-infrared spectroscopy. *Physics in Medicine and Biology*, 38(12):1859, 1993.

[70] S. A. Prahl, M. Keijzer, S. L. Jacques, and A. J. Welch. A Monte Carlo model of light propagation in tissue. *Dosimetry of Laser Radiation in Medicine and Biology*, 5:102–111, 1989.

[71] Monte Carlo eXtreme (MCX) source code. `https://github.com/fangq/mcx/tree/master/src`. Accessed: 2017-12-05.

[72] J. Chen and X. Intes. Comparison of Monte Carlo methods for fluorescence molecular tomography-computational efficiency. *Medical Physics*, 38(10):5788–5798, 2011.

[73] I. Aganj, B. T. T. Yeo, M. R. Sabuncu, and B. Fischl. On removing interpolation and resampling artifacts in rigid image registration. *IEEE Transactions on Image Processing*, 22(2):816–827, 2013.

[74] S. R. Arridge, J. P. Kaipio, V. Kolehmainen, M. Schweiger, E. Somersalo, T. Tarvainen, and M. Vauhkonen. Approximation errors and model reduction with an application in optical diffusion tomography. *Inverse Problems*, 22(1):175–195, 2006.

[75] M. Mozumder. *Image reconstruction with error modelling in diffuse optical tomography*. PhD thesis, University of Eastern Finland, Department of Applied Physics, 2015.

Appendix A

Affine transformations

Here we give the matrices corresponding to the affine transformation operations on three-dimensional points in their homogeneous coordinates. The operations include anisotropic scaling ($\mathbf{S}$), rotations with respect to the x-, y- and z-axis ($\mathbf{R}_x$, $\mathbf{R}_y$ and $\mathbf{R}_z$, respectively) and translation ($\mathbf{T}$). The positive direction of the rotations is counter-clockwise with respect to the rotation axis.

$$\mathbf{S} = \begin{bmatrix} s_x & 0 & 0 & 0 \\ 0 & s_y & 0 & 0 \\ 0 & 0 & s_z & 0 \\ 0 & 0 & 0 & 1 \end{bmatrix} \qquad \mathbf{T} = \begin{bmatrix} 1 & 0 & 0 & t_x \\ 0 & 1 & 0 & t_y \\ 0 & 0 & 1 & t_z \\ 0 & 0 & 0 & 1 \end{bmatrix}$$

$$\mathbf{R}_x = \begin{bmatrix} 1 & 0 & 0 & 0 \\ 0 & \cos r_x & -\sin r_x & 0 \\ 0 & sinr_x & \cos r_x & 0 \\ 0 & 0 & 0 & 1 \end{bmatrix} \qquad \mathbf{R}_y = \begin{bmatrix} \cos r_y & 0 & \sin r_y & \\ 0 & 1 & 0 & 0 \\ -\sin r_y & 0 & \cos r_y & 0 \\ 0 & 0 & 0 & 1 \end{bmatrix}$$

$$\mathbf{R}_z = \begin{bmatrix} \cos r_z & -\sin r_z & 0 & 0 \\ \sin r_z & \cos r_z & 0 & 0 \\ 0 & 0 & 1 & 0 \\ 0 & 0 & 0 & 1 \end{bmatrix}$$